Author Manuscript

Author Manuscript

Author Manuscript

Author Manuscript

HHS Public Access

Author manuscript

Inorg Chem. Author manuscript; available in PMC 2019 May 07.

Published in final edited form as:

Inorg Chem. 2018 May 07; 57(9): 5449–5462. doi:10.1021/acs.inorgchem.8b00419.

Direct Determination of Absolute Absorption Cross Sections at the L-Edge of Dilute Mn Complexes in Solution using a Transmission Flatjet

Markus Kubin[a], **Meiyuan Guo**[b], **Maria Ekimova**[c], **Michael L. Baker**[d], **Thomas Kroll**[e], **Erik Källman**[b], **Jan Kern**[f], **Vittal K. Yachandra**[f], **Junko Yano**[f], **Erik T. J. Nibbering**[c,*], **Marcus Lundberg**[b,*], and **Philippe Wernet**[a,*]

[a]Institute for Methods and Instrumentation for Synchrotron Radiation Research, Helmholtz-Zentrum Berlin für Materialien und Energie GmbH, 12489 Berlin, Germany

[b]Department of Chemistry - Ångström Laboratory, Uppsala University, SE-75121 Uppsala, Sweden

[c]Max-Born-Institut für Nichtlineare Optik und Kurzzeitspektroskopie, 12489 Berlin, Germany

[d]The School of Chemistry, The University of Manchester at Harwell, Didcot, OX11 OFA, U.K

[e]Stanford Synchrotron Radiation Lightsource, SLAC National Accelerator Laboratory, Menlo Park, CA 94025, USA

[f]Molecular Biophysics and Integrated Bioimaging Division, Lawrence Berkeley National Laboratory, Berkeley, CA 94720, USA

Abstract

3d transition metals play a pivotal role in many charge transfer processes in catalysis and biology. X-ray absorption spectroscopy at the L-edge of metal sites probes metal 2p-3d excitations providing key access to their valence electronic structure which is crucial for understanding these processes. We report L-edge absorption spectra of $Mn^{II}(acac)_2$ and $Mn^{III}(acac)_3$ complexes in solution, utilizing a liquid flatjet for x-ray absorption spectroscopy in transmission mode. With this we derive absolute absorption cross sections for the L-edge transitions with peak magnitudes as

*Authors to whom correspondence should be addressed: Philippe Wernet, Helmholtz-Zentrum Berlin, Albert-Einstein-Str. 15, 12489 Berlin, Germany, Tel: +49 30 806213448, wernet@helmholtz-berlin.de. Marcus Lundberg, Uppsala University, SE-75121 Uppsala, Sweden, Tel: +46-18-4713708, marcus.lundberg@kemi.uu.se Erik T. J. Nibbering, Max-Born-Institut für Nichtlineare Optik und Kurzzeitspektroskopie, 12489 Berlin, Germany. Tel: +49 30 63921477, nibberin@mbi-berlin.de.

Author Contributions

Conceived the experiment: M.K., Ph.W.
Designed the experiment: M.K., M.E., J.K., V.K.Y., J.Y., E.T.J.N., Ph.W.
Prepared the samples: M.K., M.E.
Carried out the experiment: M.K., M.E.
Analyzed the data: M.K., PhW.
Carried out ab-initio restricted active space calculations: M.G., E. K., M.L.
Carried out crystal-field multiplet calculations for Figure 5: M.K.
Carried out charge-transfer and crystal-field multiplet calculations for Figure 6: T.K., M.L.B.
Wrote the paper: M.K., Ph.W., with contributions from all authors.

Supporting Information
Data processing and analysis; details on spectrum calculations; numerical spectrum analyses.

Author Manuscript Author Manuscript Author Manuscript Author Manuscript

large as 12 and 9 Mb for $Mn^{II}(acac)_2$ and $Mn^{III}(acac)_3$, respectively. We provide insight into the electronic structure with ab-initio restricted active space calculations of these L-edge transitions, reproducing the experimental spectra with excellent agreement in terms of shapes, relative energies and relative intensities for the two complexes. Crystal field multiplet theory is used to assign spectral features in terms of the electronic structure. Comparison to charge transfer multiplet calculations reveals the importance of charge transfer in the core-excited final states. Based on our experimental observations we extrapolate the feasibility of 3d transition metal L-edge absorption spectroscopy using the liquid flatjet approach in probing highly dilute biological solution samples and possible extensions to table-top soft x-ray sources.

Graphical Abstract

We report absolute x-ray absorption cross sections at the L-edges of $Mn^{II}(acac)_2$ and $Mn^{III}(acac)_3$ complexes in solution, measured in transmission mode with a liquid flatjet. By combining ab-initio restricted active space calculations and charge-transfer multiplet theory we show the connection between electronic structure and x-ray cross sections. We extrapolate the applicability of our approach to studying metal L-edge absorption spectra of highly dilute biological solution samples and possible extensions to table-top soft x-ray sources.

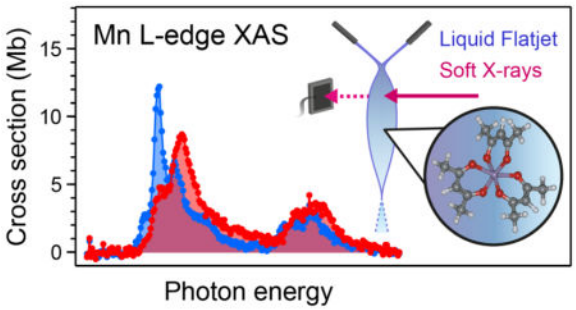

Keywords

Metal L-edge; x-ray absorption spectroscopy; transmission flatjet; absorption cross section; manganese acetylacetonate

I. Introduction

3d transition metals play an important role as electron donors or acceptors in many catalysts and metalloproteins where they facilitate charge migration and charge transfer reactions.[1–3] For a mechanistic understanding of these reactions, detailed knowledge of the local valence electronic structure at the transition metal sites is essential. X-ray absorption spectroscopy (XAS) at the metal L-edge is an ideal tool for studying this electronic structure. It directly probes the metal 3d-derived orbitals via metal-centered 2p-3d transitions being sensitive to the oxidation state and spin state of the probed metal center, as well as to the ligand environment.[4–13]

Studying the important class of solution-phase 3d transition metal complexes and catalysts with L-edge absorption spectroscopy requires special consideration for dedicated in-vacuum

Author Manuscript Author Manuscript Author Manuscript Author Manuscript

sample delivery and adapted soft x-ray detection methods. Soft x-ray absorption spectroscopy of liquid samples has been realized following different conceptual approaches. For example, liquid flow-cells based on soft x-ray transmissive membranes can be used for transmission-detected,[14–18] fluorescence yield-detected[19] and ion yield-detected XAS,[20] but their use for studying metal complexes in solution is limited due to the inherent difficulty of avoiding x-ray induced sample damage.[21–22] In a recent approach a highly sensitive photon detector was used for fluorescence-detected XAS of frozen samples, but the applicability of this approach to solution samples of dilute metal complexes at ambient conditions has not yet been proven.[23] Alternatively, Rayleigh-flow liquid jets have been developed[24] and have been used for XAS with continuous replenishment of the liquid sample.[25–26] Due to the fast sample flow through the x-ray interaction region, x-ray damage is avoided for most experiments. Since, however, the diameter of such jets is typically on the order of several tens of micrometers and therefore much larger than the typical attenuation length of soft x-rays of most solution samples, these jet systems cannot easily be used for measuring XAS in transmission mode without detrimental distortion effects. Instead, they have been mostly used for XAS in fluorescence-detected mode[11, 26–27] or for photoelectron spectroscopies.[28]

Measuring L-edge XAS in transmission mode has several advantages over the more conventional electron- or photon-yield detection methods. First, it allows for determination of absolute absorption cross sections in contrast to determination of relative cross sections with other XAS methods. This is important as it enables inter-system comparison of the metal-ligand covalency in different compounds since the integrated L-edge XAS intensities are proportional to the number of holes in the metal 3d-shell and to the metal 3d-character[7, 10, 29] (or inversely the degree of covalence bond character) of the probed valence orbitals.[30] Second, an advantage compared to detecting the partial fluorescence yield (PFY) for PFY-XAS[31] is that XAS in transmission mode is unaffected by state-dependent fluorescence yield, which can lead to relative peak intensities deviating from the cross sections due to spectrally variable intensity of the fluorescence signal.[27, 31–33]

In this paper, we demonstrate L-edge XAS in transmission mode of dilute prototypical Mn complexes in solution using a liquid flatjet system.[34] This flatjet provides a stable liquid sheet with thicknesses on the order of 1 μm, which is close to the soft x-ray attenuation length of most solvents, allowing for solution-phase soft x-ray absorption spectroscopy in transmission mode.[35–36] Flow rates on the order of 4 ml/min guarantee a continuously replenished stream of liquid sample resulting in measurements not delimited by sample damage induced by the probing x-rays. This approach offers new capabilities in the study of 3d transition metal complexes in solution.

The herein investigated prototypical high-spin $Mn^{II}(acac)_2$ and $Mn^{III}(acac)_3$ complexes in solution exhibit variable formal metal oxidation states (Mn^{II} vs. Mn^{III}) and spin states (S=5/2 vs. S=2) as well as variable metal-ligand coordination (4 vs. 6 oxygen bonds) and bonding symmetry (T_d vs. O_h/D_{4h}). With this study we complement previous work by Kubin et al.[13] on these complexes where L-edge PFY-XAS was used to investigate the origin of the L_3-edge spectral shift between the Mn^{II} and Mn^{III} species. Here we focus on the comparison of absolute absorption cross sections of L-edge XAS, on the interpretation of selected spectral features, and on the comparison of spectra from XAS and from PFY-XAS. We

Author Manuscript Author Manuscript Author Manuscript Author Manuscript

compare our experimental spectra to those calculated with the widely used crystal-field multiplet (CFM) and charge-transfer multiplet (CTM) methods,[7, 37–38] to ab-initio calculations based on the restricted active space (RAS) approach.[39–44] We conclude our study with an assessment of alternative applications of our experimental approach, namely for studying highly dilute biological systems and for using our approach with table-top soft x-ray sources.

II. Materials and Methods

Sample Preparation

$Mn^{III}(acac)_3$ (Manganese(3+) tris[(2Z)-4-oxo-2-penten-2-olate]), acetylacetonato ligands are abbreviated as $(acac)^-$), and $Mn^{II}(acac)_2$ (Manganese(2+) bis[(2Z)-4-oxo-2-penten-2-olate]) were purchased as crystalline powders (technical grade) from Sigma-Aldrich and were used without further purification. They were dissolved in ethanol abs. (≥99.8% purity, Sigma-Aldrich) with concentrations of 100 mM and 15 mM for $Mn^{III}(acac)_3$ and of 30 mM for $Mn^{II}(acac)_2$. Solutions were filtered with 0.45 μm PTFE Whatman™ filters before the measurements. Exposure to oxygen and ambient light was minimized during sample preparation and sample injection.

Experimental Setup and Data Analysis

All experiments were performed with the recently reported transmission flatjet setup[34] at the undulator beamline UE52-SGM[45] of the BESSY II synchrotron radiation facility. A schematic side view of the setup is given in Figure 1A. Two sample flasks, one with pure solvent ethanol and one with ethanol solution of the studied Mn complex, were connected to the switching unit (Jasco LG-2080-02S). An HPLC pump (Jasco PU-2085-Plus) injected the selected liquid sample into the x-ray probing region at pressures between 3.0 and 4.0 MPa, keeping the flow rate at a fixed value of 3.4 ml/min. The flatjet was formed by two colliding jets (inner nozzle diameters 48 μm) resulting in a primary liquid sheet formation with typical horizontal and vertical extensions of ~1 mm and ~ 3 mm, respectively. The thickness of the liquid sheet changes between 0.5 and 3.5 μm on a mm length scale within the first sheet,[34, 36] but is constant in the range of the x-ray spot diameter of approximately 60 μm.[45] The sheet was placed in the focus of the x-ray beam and horizontally centered with respect to the probing x-ray spot and vertically adjusted for the desired effective thickness. The recycling unit introduced in ref.[34] was not used. Instead, we trapped the liquid sample at 77 K below the x-ray probing region, which allowed for working pressures around $\sim 10^{-3}$ mbar in the experimental chamber. The experimental chamber was separated from the beamline with a differential pumping stage to warrant appropriate vacuum conditions for both the beamline and the experimental chamber. The primary sheet of the liquid flatjet was typically probed here at thicknesses between 2.5 μm and 3.2 μm. The photon flux $\Phi_L(h\nu)$ transmitted through the sample was recorded as a function of the photon energy by a calibrated photodiode (Hamamatsu G1127-04 2K) that was positioned on the x-ray beam axis at ~0.4 m distance from the liquid jet and was read out by a Keithley Electrometer (model 6514B). The noise level of this transmitted flux strongly depends on the stability of the transmission flatjet and was measured around 0.1 % for the most stable jet and around 0.6% for rather unstable jet conditions. The photon flux $\Phi_0(h\nu)$ incident on the sample (I_0) was scanned separately, after

Author Manuscript Author Manuscript Author Manuscript Author Manuscript

removing the liquid jet from the x-ray beam. The noise of this signal was determined around 0.1%. The transmission spectra were eventually obtained from the quotient $T_L(h\nu) = \Phi_L(h\nu)/\Phi_0(h\nu)$. Further details of the setup can be found in ref.[34].

For a spectrum scan, the monochromator was scanned in steps of 0.1 eV (1 s integration time per step) over the Mn L-edge region (630–660 eV). The O K-edge region (500–700 eV) was scanned (in 1 eV steps) to determine the sheet thickness with tabulated O K-edge absorption cross sections from Henke's tables.[46–47] Typical acquisition times for a single-scan spectrum were around 10 min. The monochromator slit size was set to 120 μm or 150 μm, corresponding to bandwidths of 300 meV or 380 meV, respectively, at the Mn L-edge. The beamline flux was on the order of 1×10^{12} photons/s (diode current ~20 μA) in the Mn L-edge spectral region. In case the spectrum and reference scans were recorded with different monochromator slit sizes w_s and w_0, respectively, the reference signal was rescaled with a linear factor w_s/w_0. This procedure was checked for consistency as shown in the Supporting Information (S.I.), section 1.1.

All diode signals were normalized by the storage ring current of the BESSY II synchrotron radiation facility. As in refs.[12–13], we have calibrated the axis of the incident photon energy to the L_3-edge maximum of a Mn^{2+}_{aq} solution sample with a relative uncertainty of 50 meV with respect to the values reported in ref.[48] via the sharp Mn^{II} L_3 peak position at 639.7 eV. The incident x-ray flux was found to decrease with respect to time due to an increasing portion of the beam being clipped by the experimental chamber (see S.I., section 1.2.2 for details). We corrected for this in the data analysis with a spectrally constant attenuation factor *Att.* ($0.4<Att.\leq1$) which reduces the original incident flux $\Phi_0(h\nu)$ to $\Phi_{Att.}(h\nu) = Att\cdot\Phi_0(h\nu)$. We retrieved this factor *Att.* from a least-squares fit of the uncorrected experimental transmission of the solvent to that expected from tabulated values.[46–47] From the same fit of transmission spectra $T_L(h\nu)$, with fit parameters *Att.* and the sample thickness *L*, we retrieved the effective sample thickness for each spectrum scan. The fit regions were chosen such that no absorption resonances were included (see S.I., section 1.2.1). All transmission curves and further processed spectra shown in this paper were corrected by this fitted attenuation factor *Att.*. We note that with this procedure we lose information about the spectral intensity of the edge-jump on the high-energy side of the Mn L-edge absorption spectra. Further details on the data analysis are summarized in the S.I., section 1.

Density Functional Theory (DFT)

The molecular structures used for the restricted active space calculations (see below) were obtained from ground state density functional theory (DFT) calculations (using a DFT/B3LYP solvent optimization). The same geometries were also used for the RAS calculations in ref.[13]. The molecular structures of the two complexes are displayed in Figures 1B and 1C, where $Mn^{II}(acac)_2$ and $Mn^{III}(acac)_3$ have a nearly tetrahedral (T_d) Mn-O coordination symmetry and a Jahn-Teller distorted nearly D_{4h} Mn-O coordination symmetry[49–50], respectively. The structure of $Mn^{III}(acac)_3$, as reported in crystallographic investigations,[51] comprises four short and two long Mn-O bond lengths of 1.935 and 2.11 Å. These agree well with our calculated bond lengths of 1.93/1.94 Å and 2.17 Å, with a slight

Author Manuscript Author Manuscript Author Manuscript Author Manuscript

overestimation of the long distances consistent with previous experience.[52] Concerning the molecular structure of $Mn^{II}(acac)_2$ we are not aware of any crystallographic data since the compound crystallizes as $Mn^{II}(acac)_2$ trimers.[53] The reported crystal structure of such $Mn^{II}(acac)_2$ trimers exhibits a trigonal-prismatic D_{3h}-O_h-D_{3h} structure, resulting in a six-coordination of each Mn by six O atoms in a near octahedral geometry and Mn-O bond lengths between 2.1 and 2.2 Å.[53] Our Mn-O bond lengths of 2.06 Å for $Mn^{II}(acac)_2$ are consistent with this.

Restricted Active Space (RAS) Calculations

Ab-initio methods are uniquely beneficial compared to semi-empirical methods such as the crystal-field multiplet approach since they provide valuable predictive character and access to the spatially resolved charge and spin in the probed molecule.[13] The restricted active space (RAS) approach has been shown to correctly treat the individual many-electron interactions contributing to K-edge spectroscopies[54–55] and Ledge spectroscopies involving the interactions with the 2p core hole.[11, 13, 39–40, 43, 56] The ab-initio theoretical L-edge spectra presented here were obtained from RAS calculations including dynamic correlation performed with MOLCAS 7.9[57] at the RASPT2/ANO-RCC-VTZP level[13, 42] (the sensitivity of the RAS results to different model choices is analyzed in ref.[58]). The RAS calculations are based on the molecular geometries from the DFT/B3LYP solvent optimizations of the two complexes (see above). To save computational cost, the calculations for $Mn^{III}(acac)_3$ were performed on a truncated complex where six terminal methyl groups were replaced by hydrogen atoms, which did not notably change the spectrum. All calculations were performed in a solvent environment that was modeled using the polarized continuum model (PCM) for the solvent ethanol. In the RAS calculations, a minimal active space consisting of the five metal-3d dominated orbitals were placed in the RAS2 space. The Mn 2p orbitals were placed in the RAS3 space, allowing a maximum of five electrons (at least one hole) in the core excited states. All possible configurations that represent single core excitations were included. For $Mn^{II}(acac)_2$, 4;4;3;4 sextet states, 37;37;39;37 quartet states, and 72;72;69;72 doublet states were included for the a_1; b_1; a_2; b_2 irreducible representations in C_{2v} symmetry. For $Mn^{III}(acac)_3$, 1;2 septet, 37;38 quintet, 147;150 triplet and 111;114 singlet core-excited states were included for the two irreducible representations (a;b) in C_2 symmetry. To ensure that the hole is located in the Mn 2p orbitals (instead of the Mn 3p orbitals, upon ‘orbital rotation’), these orbitals were frozen in the RASSCF optimizations. RASPT2 calculations were performed using the default ionization potential electron affinity (IPEA) shift of 0.25 Hartree and an imaginary shift of 0.1 Hartree to reduce the occurrence of ‘intruder states’ in the core-excited states. Unlike in ref.[44], including dynamic correlation effects within the RASPT2-approach improved the spectrum quality of the Mn^{III} complex significantly as compared to RASSCF calculations (see Figure S9 in the S.I.). RAS spectra were calculated for T=300 K and were broadened with a Gaussian broadening of σ= 0.127 eV (0.3 eV FWHM) and 0.2 eV and 0.7 eV Lorentzian lifetime widths (FWHM) for the L_3 and L_2 edges, respectively.[59] This approach is the same as for the theoretical RAS spectra given in ref.[13]. For comparison to the calculated spectra in ref.[13] we checked that changing the solvent from acetylacetone to ethanol has no effect on the calculated L-edge spectra (shape and energies of the spectra are indistinguishable for the different solvents described with continuum polarization models). The calculated incident photon energy axis was

Author Manuscript Author Manuscript Author Manuscript Author Manuscript

corrected to match experimental energies. The same shift of −3.09 eV was applied to the XAS spectra of both $Mn^{II}(acac)_2$ and $Mn^{III}(acac)_3$ calculated with RAS for matching the experimental L_3-edge maximum in $Mn^{II}(acac)_2$ from ref.[13].

CFM and CTM Multiplet Theory

Crystal field multiplet (CFM)[37] and charge transfer multiplet (CTM)[38] calculations can provide important insights to the influence of specific effects to L-edge XAS, as they enable for systematically varying and "switching on and off" relevant interactions in L-edge XAS.[7, 10, 37–38] CFM and CTM calculations of Mn L-edge spectra were implemented using the multiplet program by Thole et al.[60] and the CTM4XAS interface.[61] All spectra were calculated for T=300 K. CFM and CTM spectra were broadened with 0.2 eV and 0.7 eV Lorentzian lifetime widths (FWHM) for the L_3 and L_2 edges, respectively,[59] and a Gaussian broadening of σ= 0.127 eV (0.3 eV FWHM) throughout, unless further specified. All CFM and CTM calculations are based on Slater integrals that were reduced to 80% of their Hartree-Fock atomic values. All CFM and CTM fit parameters are given in Table S1 in the S.I.. The parameters for the CTM fits of XAS are equivalent to those applied for the CTM fits of PFY-XAS spectra shown in ref.[13]. The energy axes of the final CFM and CTM spectra are corrected by constant offsets such that the L_3-edge maximum position coincides with that of the experimental spectrum, unless indicated otherwise. Shifts of −0.7 eV and −0.5 eV were applied to all CFM spectra of Mn^{2+} in tetrahedral (T_d) and Mn^{3+} in octahedral (O_h) symmetry, respectively, for all values of 10 Dq, to align the L_3-edge maxima of the best-fitting spectra to those in the experimental spectra. All CFM spectra of Mn^{2+} and Mn^{3+} calculated in D_{4h} symmetry were aligned to the L_3-edge absorption maxima of the experimental spectra.

III. Results and Discussion

Transmission XAS of Dilute Metal Complexes in Solution

In Figures 1D and 1E we show typical transmission spectra of $Mn^{II}(acac)_2$ at a concentration of 30 mM in ethanol. Fig 1E is a zoom of Figure 1D into the Mn L-edge spectral region. All transmission spectra in Figures 1D and 1E were normalized to the thickness L of a pure solvent ethanol sample (orange curve) at 2.44 μm, using Beer-Lambert's law $T_L(h\nu) = \exp(-L/\Lambda(h\nu)) = \exp(-\alpha(h\nu)\cdot L)$, where $h\nu$ is the incident photon energy, $\Lambda(h\nu)$ is the attenuation length and $\alpha(h\nu) = \Lambda^{-1}(h\nu)$ is the linear absorption coefficient.

The comparison of transmission curves for only the solvent (orange and black solid curves in Figures 1D and 1E) and for solution samples including the $Mn^{II}(acac)_2$ solute (solid blue curve in Figures 1D and 1E) illustrate that for organic solvents the spectral transmission in the soft x-ray range is governed by the light elements (here predominantly O K-edge absorption) of the solvent. The L-edge absorption signal of the dilute Mn complex represents small additional dips. This signal corresponds to the Mn $2p^63d^n \rightarrow 2p^53d^{n+1}$ absorption resonances with excitations to core-excited states where a Mn 2p electron is promoted to the 3d-derived orbitals. These resonances group into the Mn L_3- and L_2-edges, which are split by around 10 eV due to spin-orbit interaction in the presence of the 2p core hole in the XAS final states.[62] Figure 1E reveals a splitting of each of the two L-edge features which is

Author Manuscript Author Manuscript Author Manuscript Author Manuscript

caused by crystal field atomic multiplet effects as well as charge-transfer interactions of the probed Mn atoms with the ligand oxygen atoms. We will address the details of these absorption features below.

In Figure 2 we compare single-scan spectra of samples with variable concentrations of 0 mM (solvent only), 15 mM and 100 mM $Mn^{III}(acac)_3$ in ethanol. In Figure 2A, transmission spectra are shown, illustrating the influence of the solute concentration on the amplitude of the Mn L-edge spectral dip with respect to the overall transmission. The non-resonant parts of the spectra at 500–530 eV, 560–638 eV, and 658–700 eV were fitted with the tabulated transmission of the solvent ethanol(dotted lines).[46–47] This provides the crucial information of the employed sample thickness thereby determined to 2.5 μm, 2.9 μm, and 2.7 μm from top to bottom (see Materials and Methods and the S.I., section 1.2, for details). The dip amplitude of the Mn L_3-edge maximum increases when going from the 15 mM to the 100 mM sample (Mn L-edge absorption is evidently absent in the pure solvent). Figure 2B displays the corresponding linear absorption coefficients $\alpha(h\nu)$ of solute and solvent as calculated using Beer-Lambert's law with the measured properties $T_L(h\nu)$ and L.

In Figure 2C we show the relative transmission dips due to Mn L-edge absorption, that were obtained from division of the experimental transmission curves (Figure 2A) by the fitted solvent transmission (Figure 2A dotted curves). The peak amplitude of the relative transmission dips at the Mn L_3-edge increases from 3% to 12% when going from the 15 mM to the 100 mM sample. In Figure 2D we display the linear absorption coefficient $\alpha(h\nu)$ due to Mn L-edge absorption of only the solute. These curves were obtained from subtraction of the fitted solvent signal from the experimental curves in Figure 2B. The linear absorption coefficients of Mn peak around $1{\cdot}10^4$ m^{-1} and $5{\cdot}10^4$ m^{-1} for the 15 mM and 100 mM samples, respectively. The experimental ratio of peak intensities for the two single-scan spectra is around 5 and, thus, smaller than the expected ratio of 6.7 (=100/15). This deviation reflects the experimental uncertainties discussed in the following section.

Absolute X-ray Absorption Cross Sections

For an arbitrary solution sample containing *i* different molecular or atomic species with respective concentrations c_i, Beer-Lambert's law connects the experimental linear absorption coefficient $\alpha(h\nu)= \Sigma_i \alpha_i$ to the absorption coefficients α_i and absorption cross sections $\sigma_i(h\nu)$ of the individual species *i* via $\alpha(h\nu) = \Sigma_i c_i{\cdot}N_A{\cdot}\sigma_i(h\nu)$, where N_A is Avogadro's number. With this we retrieve the final absorption cross-section spectra in units of Mb (1 $b=10^{-28}$ m^2), being thus independent from the experimental parameters.

These absorption cross section spectra of $Mn^{II}(acac)_2$ and $Mn^{III}(acac)_3$ are shown in Figure 3A. The $Mn^{II}(acac)_2$ spectrum (blue) is averaged from 8 successive single-scan spectra (30 mM concentration). The $Mn^{III}(acac)_3$ spectrum (red) is averaged from 13 single-scan spectra of $Mn^{III}(acac)_3$ (two scans of a 100 mM sample and eleven runs of a 15 mM sample). The total acquisition time amounts to ~1.5 and ~2.5 hours for the averaged spectra of Mn^{II} and Mn^{III}, respectively.

The direct comparison of the spectra in Figure 3A leads to a number of observations. First, the L_3-edge absorption maxima are shifted in energy with respect to each other by 1.9 eV.

Author Manuscript Author Manuscript Author Manuscript Author Manuscript

This agrees with the shift of 2.0 eV determined in a previous study of L-edge PFY-XAS spectra of $Mn^{II}(acac)_2$ and $Mn^{III}(acac)_3$ (ref.[13]). The shift is interpreted as a final state effect due to an increased affinity to 3d electrons in the core-excited XAS final states. Similar spectral shifts between 1.5 and 2 eV have been reported for other series of high-spin Mn complexes with various oxidation states.[4, 12] A second observation concerns differences in the absolute absorption cross sections and associated absorption integral of the two molecular species. This provides quantitative information which is difficult to access in fluorescence yield detected XAS due to state-dependent fluorescence yield and which complements electron-yield detected XAS[7]. With 12.4±1.0 Mb the L_3-edge peak maximum of the Mn^{II} species is about 40% more intense than that of Mn^{III} at 8.8±1.9 Mb. The error bars reflect a combination of systematic uncertainties of the sample concentrations due to precipitation and statistical errors due to fluctuations in the jet thickness (see Figure S8 in the S.I.). Concomitant to the lower intensity at the L_3-edge maximum the $Mn^{III}(acac)_3$ spectrum appears broader with a more extended intensity distribution as compared to $Mn^{II}(acac)_2$. These differences in shape are a direct consequence of the increasing multiplet interactions when going from Mn^{II} to Mn^{III} (see refs.[62–63]). With absolute cross sections we can also compare integrals of the L-edge absorption spectra for the two complexes. The total L-edge intensity is interpreted as proportional to the number of holes in the 3d-derived valence orbitals and their associated covalency[7]. Obtaining the integrated intensity in Mb·eV can therefore reveal information on the occupation number of these valence orbitals. We find (for integration over the full energy range shown in Figure 3A) absorption integrals of 48±11 Mb·eV for $Mn^{III}(acac)_3$ and 41.5±3.3 Mb·eV for $Mn^{II}(acac)_2$. The error bars reflect the uncertainty of the cross sections claimed above and comprise systematic uncertainties due to differences in the background subtraction scheme (linear background as applied here vs. edge-jump background as applied in ref.[7]). The ratio of our experimental spectrum areas is 1.16±0.28 for Mn^{III}/Mn^{II} and reflects the ratio of Mn^{III}/Mn^{II} 3d holes with 6/5=1.2 for Mn^{III}/Mn^{II} as expected for the Mn^{III}/Mn^{II} ground state configurations $3d^4/3d^5$ with small contributions of metal-ligand covalent interactions. Within the error bars the experimental ratio therefore reflects the predominantly ionic character of Mn in $Mn^{III}(acac)_3$ and $Mn^{II}(acac)_2$. The transmission-mode spectra shown here thus allow to directly confirm simple but important expectations for L-edge XAS of Mn^{II} and Mn^{III} complexes: The overall spectrum intensity increases due to the increasing number of 3d holes but it is spectrally redistributed when going from Mn^{II} to Mn^{III} due to increasing multiplet splittings. The results of the numerical analyses in this paragraph are summarized in Table S2 in the S.I..

In experiments with smaller uncertainties in the Mn cross sections, transmission-mode measurements could be applied for the determination of the metal character (the degree of covalence) of the probed metal 3d-derived valence orbitals. This direct way of probing the relative number of holes in the metal 3d-derived orbitals with L-edge XAS is complementary to probing the relative number of electrons in the 3d-derived molecular orbitals via their np-character with valence-to-core $K\beta_{2,5}$ XES.[64] Beckwith et al. report a ratio of 1.45±0.10 for the spectrum areas of valence-to-core emission signals of $Mn^{III}(acac)_3$ as compared to $Mn^{II}(acac)_2$.[65] The discrepancy of this number with the expected ratio of electrons in the 3d-derived orbitals in the respective ground states (4/5=0.8 for Mn^{III}/Mn^{II})

Author Manuscript Author Manuscript Author Manuscript Author Manuscript

was explained by the shorter Mn-ligand bond lengths in $Mn^{III}(acac)_3$ which "provide a mechanism for increased Mn-np mixing into the ligand orbitals".[65] This points to a difference in the complementary sensitivity between L-edge XAS and $K\beta_{2,5}$ XES to metal-ligand bond lengths and orbital admixtures. In contrast to XES-based methods which probe differences in the ligand p-character of the 3d-derived orbitals, metal L-edge XAS provides a direct way for probing the metal-d character of the metal 3d-derived valence orbitals.

Absence of X-ray Induced Sample Damage

Due to their ionizing character, soft x-rays tend to modify the chemical structure of the probed samples. A major source of x-ray induced sample damage is the vast amount of electrons and radicals created upon ionization of the sample. X-ray spectroscopic signatures of such "beam damage" appear, for example, via the signature of a chemically reduced species. For a Mn^{III} sample one would expect the signature of a Mn^{II} species to appear in considerable amounts at x-ray doses on the order of 10^6 Gy.[21–22] In case of insufficiently replenished samples such doses can quickly be reached at typical synchrotron radiation beamlines. For our experiment we estimate that the doses absorbed by the flatjet samples are on the order of ~20 Gy and thus five orders of magnitude below the critical threshold. We conclude that with our transmission flatjet we measure spectra unaffected by (dose-dependent) x-ray induced sample damage. We note that this could not be ensured in earlier L-edge spectroscopic studies of non-replenished solid $Mn^{III}(acac)_3$ samples.[66–67] Confirming results from ref.[13], the much broader L_3-edge of the $Mn^{III}(acac)_3$ spectrum in refs.[66–67] compared to the spectrum reported here with considerable intensity at the peak location characteristic for Mn^{II} species indicates that the spectra in refs.[66–67] suffer from x-ray induced sample damage. We roughly estimate the relative Mn^{II} content in these experiments to several 10%.[66–67] Based on one of these sets of spectra recent restricted open-shell configuration interaction singlet (ROCIS) simulations of metal L-edge XAS of $Mn^{II}(acac)_2$ and $Mn^{III}(acac)_3$ show differences to both our experimental and RAS calculated spectra.[68–69]

Spectrum Calculations with RAS

In Figure 3B we show Mn L-edge XAS spectra of $Mn^{II}(acac)_2$ and $Mn^{III}(acac)_3$ in ethanol solution as calculated with RAS theory, based on the molecular structures shown in Figures 1B and 1C. The relative energies and intensities of the two complexes are displayed as calculated. We find excellent agreement with our experimental spectra with respect to the overall shapes, the relative peak positions and the relative peak intensities in the individual spectra. The RAS spectra nicely reproduce the sharp and intense L_3-edge peak in $Mn^{II}(acac)_2$ as compared to the broad and less intense L_3-edge peak in $Mn^{III}(acac)_3$. The L_3-edge shift is underestimated by the RAS calculations by 16% (1.6 eV from RAS as compared to 1.9 eV from the experiment). The relative peak absorptions of Mn^{III} and Mn^{II} are reproduced within the experimental error bars by the ratio of 0.69 in the RAS calculations as compared to the experimental ratio of 0.71±0.15. The calculated ratio of 1.29 of the Mn^{III}/Mn^{II} spectrum areas from RAS is also within the experimental limits of 1.16±0.28 (see also Table S2 in the S.I.).. This indicates that the differences between the two complexes in terms of electronic structures and atomic multiplet effects are well accounted for in the RAS calculations.

Author Manuscript Author Manuscript Author Manuscript Author Manuscript

In Figures 4A and 4B we compare calculated and measured spectra in more detail by also including the individual transitions as sticks in the calculated spectra. The agreement between calculated and measured spectra illustrates the quality of such state-of the art RAS spectral calculations. Overall the calculated spectral features appear too narrow compared to experiment and this could be due to the neglect of inhomogeneous broadening by structural fluctuations in the calculations. The largest discrepancies between theory and experiment, however, appear in the spectrum of $Mn^{II}(acac)_2$ between 641 and 644 eV, where the intensity is underestimated in the calculated spectrum, and, to a lesser extent, in the same region in the $Mn^{III}(acac)_3$ spectra. These high-energy sides of the L_3-edges were characterized before in Fe L-edge XAS as arising from excitations to charge-transfer (CT) states.[7] At this point we can only speculate that the missing intensity in our RAS calculations is due to missing CT excitations as they include only the five active orbitals with metal 3d character and therefore do not take into account excitations to ligand-dominated orbitals, as required to describe the CT final states. RAS calculations can easily be extended with another five or even more valence orbitals. However, for ionic complexes the minimal active space of five metal 3d-derived orbitals is the most stable, ensuring consistent comparisons between the two complexes. Alternative implementations of ab-initio type calculations of L-edge XAS may include many more final states with CT character[70] and comparisons of the different approaches promises further insight.

$L_{3,2}$-edge Branching Ratios

The proportion of integral absorption areas of the Mn L_3 and L_2-edges in the spectra is often denoted the “branching ratio” (see refs.[63, 71]). It reflects the statistical ratio of $2p_{j=3/2} \rightarrow 3d$ and $2p_{j=1/2} \rightarrow 3d$ transitions where *j* denotes the total angular momentum of the 2p hole. We determine the L_3 and L_2 absorption integrals over the energy ranges $h\nu<647.5$ eV and $h\nu>647.5$ eV for the Mn L_3 and L_2-edges, respectively, and obtain experimental branching ratios $L_3/(L_3+L_2)$ of 0.72±0.02 for $Mn^{II}(acac)_2$ and 0.66±0.02 for $Mn^{III}(acac)_3$. The error bars account for the estimated deviation of branching ratios after linear background subtraction (as applied here) with respect to subtraction of an $L_{3,2}$-edge jump as applied in ref.[7]. These values agree well with those calculated in ref.[63] by Thole and van der Laan stating average branching ratios of 0.74 and 0.66 for atomic Mn^{II} and Mn^{III}, where a typical reduction factor 0.75 was applied to all Slater integrals.

The branching ratio extracted from the calculated RAS spectrum of $Mn^{II}(acac)_2$ amounts to 0.78 and thus significantly deviates from the experimentally determined branching ratio of 0.72 ±0.02. This reveals an overestimation of the L_3-edge intensity (or equivalently an underestimation of the L_2-edge) in the calculated with respect to the experimental spectrum. In contrast, for $Mn^{III}(acac)_3$ good agreement is found for the branching ratio of 0.65 in the RAS spectrum to that from experiment (0.66±0.02). The reason for the limited capability of RAS to consistently reproduce the branching ratio of Mn^{II} is not well understood, but could possibly be due to the perturbative treatment of the strong 2p spin-orbit coupling.

CFM Theory for Variable Ligand Field Splittings 10 Dq

We use CFM calculations for a systematic study of the influence of the ligand field splitting 10 Dq in a cubic ligand environment on the L-edge XAS spectrum and we use the

Author Manuscript Author Manuscript Author Manuscript Author Manuscript

comparison of CFM and CTM to investigate the influence of CT states on the spectra. In Figure 5 we compare the experimental spectra to a series of theoretical spectra calculated with the CFM approach in T_d/O_h symmetry where we vary the ligand field splitting parameter 10 Dq. We track the energies of corresponding multiplet features with gray lines as 10 Dq is systematically increased.

The spectrum of $Mn^{II}(acac)_2$ in Figure 5 is qualitatively well described by the spectral multiplet features of a field-free Mn^{2+} ion (with 10 Dq=0). Apparently, however, no such agreement is found for the spectrum calculated for the field-free Mn^{3+} ion when compared to the experimental $Mn^{III}(acac)_3$ spectrum. Varying 10 Dq illustrates the influence of the Mn-O coordination geometry on the electronic structure[72] and, more specifically, on the spectrum observable in Mn L-edge XAS.[37] For Mn^{2+} a weak pre-edge peak below the L_3-edge in Figure 5 splits off on the low energy side of the main L_3-edge maximum with increasing separation as 10 Dq is increased. With respect to this pre-edge peak, the best qualitative match to the experimental spectrum is found for 10 Dq=0.6 eV. Moreover, all other peaks in the L_3-edge seem to broaden when 10 Dq is increased. Varying 10 Dq for Mn^{3+} leads to dramatic redistribution of intensities in the spectra and, in particular, to the appearance of a strong pre-edge feature on the low energy side of the L_3-edge. The best qualitative match with experiment is found for 10 Dq=1.5 eV (the calculated CFM(T_d/O_h) spectra with shapes best matching experiment are marked with arrows in Figure 5). For both complexes these are the values where the L_3 pre-edge features and the “smooth” intensity distribution on the high-energy side of the L_3-edge best match those in the experimental spectra. Both observables seem to characteristically correlate with the values of 10 Dq. In particular the presence of a strong pre-edge feature at 1 to 2 eV below the L_3-edge maximum appears to be characteristic for the octahedral complex.

We can assess the fit results with information on the ligand field strength from UV-vis spectroscopic investigations where for $Mn^{III}(acac)_3$ optical absorption energies between 2.1 and 2.4 eV have been found for the $^5T_{2g} \rightarrow {}^5E_g$ transitions.[73–74] This is roughly consistent with our approximate value for the ligand-field splitting of 10 Dq=1.5 eV found for Mn^{3+} in $Mn^{III}(acac)_3$. The 30–40% smaller value of 10 Dq from CFM theory compared to UV-vis may be explained with an “increased localization of the 3d states in the presence of the core hole” (ref.[4] and ref.17 therein). We are not aware of any UV-vis data or values of the ligand field splittings in $Mn^{II}(acac)_2$ to which we could reference our value of 10 Dq, but the value is consistent with crystal-field theory that predicts 10 Dq of tetrahedral complexes to be 4/9 of the value of corresponding octahedral complexes.[72]

We note that the simulated CFM spectra in Figure 5 for octahedrally coordinated Mn^{III} with 10 Dq changing from 2.7 eV to 3.0 eV illustrate the effect of an abrupt transition from a high-spin to a low-spin Mn^{3+} complex with S=2 and S=0 ground states, respectively. This is where the multiplet structures in both the L_3 and L_2-edges abruptly change. Such a high-spin to low-spin transition was reported to occur at around 10 Dq=3 eV for octahedrally coordinated Mn^{3+} (and also for tetrahedrally coordinated Mn^{2+}).[62] The CFM analysis can therefore be used to confirm the spin states of the Mn^{II} and Mn^{III} species in the ground states of $Mn^{II}(acac)_2$ and $Mn^{III}(acac)_3$ to be high spin.

Author Manuscript Author Manuscript Author Manuscript Author Manuscript

With the above analysis we have identified the occurrence of a strong (weak) pre-edge feature at 1 to 2 eV below the L_3 absorption maximum to be characteristic for Mn coordinated in octahedral (tetrahedral) ligand fields. A similar yet more distinct pre-edge feature was observed by Pinjari et al.[40] in L-edge XAS of both high-spin and low spin Fe^{3+} ions in octahedral ligand fields (Fe^{3+} is isoelectronic to Mn^{2+} and has a similar L-edge spectral shape). In ref.[40] the calculated RAS ligand field is represented once by point charges and once by molecular ligands. The orbital-population analysis of these RAS spectra reveals differences in the assignment of the pre-edge feature. Importantly, for the high-spin Fe^{3+} ion in a point charge field, the pre-edge feature is predominantly assigned to one-electron transitions to the energetically low-lying t_{2g}-orbitals, while in the example of a molecular high-spin Fe^{3+} complex this assignment breaks down due to strong mixing of orbital contributions in the pre-edge feature. This latter observation agrees with findings from analyses of RAS calculated L-edge XAS spectra of $Mn^{II}(acac)_2$ and $Mn^{III}(acac)_3$ for orbital populations in the core-excited states[13] where no particular assignment of peaks to specific orbital-excitations was found.

Spectrum Fits using CFM and CTM Theory

In Figure 6 we compare the best fitting CFM(T_d/O_h) spectra from Figure 5 to more quantitative multi-parameter fits that we performed within the CFM and CTM frameworks. With respect to the CFM model the CTM approach uses a valence bond configuration interaction model to include charge transfer (CT) states with energy separations Δ_{CT} and mixing parameters T.[8] The CFM and CTM multi-parameter simulations were implemented in D_{4h} symmetry where additional parameters D_s and D_t include the energy splittings due to Jahn-Teller distortion.

In Figure 6 we observe that the best fitting spectra from our single-parameter CFM(T_d/O_h) fits show strong similarity to the spectra obtained from the multi-parameter CFM(D_{4h}) fits, yet with better qualitative agreement to the experimental spectra of $Mn^{II}(acac)_2$ and $Mn^{III}(acac)_3$. This concerns in particular the shape of the pre-edge features in both spectra. Yet, even better agreement to the experimental spectra is obtained for the CTM(D_{4h}) fits which involve up to 10 free parameters (see fit parameters in Table S1 in the S.I.), in particular for modeling the charge transfer states. The CTM model adds a $d^{n+1}\underline{L}$ configuration to the single configuration ground state d^n and $\underline{c}d^{n+2}\underline{L}$ to the $\underline{c}d^{n+1}$ configurations in the core-excited XAS final states (where $\underline{L}$ and $\underline{c}$ denote holes in the ligand and in the 2p core orbitals, respectively). This is known to produce CT excitations or CT core-excited states (shake-up states) to the high-energy side of the L_3 and L_2 edges, respectively.[7–8, 10] Inclusion of charge transfer states improves the agreement of the calculated Mn^{II} spectrum at the “smooth” high-energy side of the L_3-edge (641–647 eV) with the experimental spectrum of $Mn^{II}(acac)_2$ (Figure 6A). Apparently, CT states add intensity in this spectral range which explicitly cannot be reproduced neither with the purely ionic CFM calculations nor with our RAS calculations. The CTM fit for Mn^{III} in $Mn^{III}(acac)_3$ in Figure 6B also shows a smoother flank on the high-energy side of the L_3-edge (642–647 eV) as compared to the CFM and the RAS calculations and in good agreement with the experimental spectrum.

Author Manuscript Author Manuscript Author Manuscript Author Manuscript

The branching ratios of the $Mn^{III}(acac)_3$ CFM(D_{4h}) and CTM spectra amount to 0.65 and 0.67, respectively, which is in good agreement with the experimental value of 0.66±0.02. However, both CFM and CTM calculations overestimate the branching ratio in the spectrum of the $Mn^{II}(acac)_2$ complex (0.76 and 0.75 for CFM(D_{4h}) and CTM, respectively, as compared to 0.72±0.02 from experiment). This trend is the same as in the RAS calculations. We observe that for both systems including CT states affects the branching ratios only marginally.

Comparison to Partial Fluorescence-Yield XAS

In transmission mode XAS the $2p^63d^n \rightarrow 2p^53d^{n+1}$ transitions (and their cross sections) are probed most directly, whereas PFY-XAS, measuring 3d-2p fluorescence intensity, introduces state-dependent fluorescence yield effects[27, 31–33] due to spectrally variable fluorescence decay of core-excited XAS final states $2p^53d^{n+1}$ to valence excited PFY-XAS final states $(2p^63d^n)^*$. In Figures 7A and 7B we illustrate these effects by comparing the absorption spectra of $Mn^{II}(acac)_2$ and $Mn^{III}(acac)_3$ from transmission detected XAS with respect to PFY-detected XAS from ref.[13]. Note that the same absolute energy calibration for all experimental spectra was used and all spectra were normalized to the same intensity at the L_3 edge maximum. We identify almost all features of the transmission XAS spectra also in the PFY-XAS spectra and for each complex the specific energy of the features agree well.

The most apparent difference between the two detection modes is the enhancement or suppression of individual spectrum features due to state-dependent fluorescence yield. With all spectra normalized to their maximum intensity, for both complexes, this is most pronounced in a relative enhancement of the L_2-edge with respect to the L_3-edge in PFY-XAS as compared to transmission XAS. Quantitatively, in PFY-XAS the branching ratios for $Mn^{II}(acac)_2$ and $Mn^{III}(acac)_3$ are 0.49 and 0.50 as compared to 0.72 and 0.66 in transmission XAS, respectively. These observations of state-dependent fluorescence yield are consistent with earlier studies.[31–33, 48]

Based on CFM analyses, Miedema et al. find that the 2p-3d exchange interaction in the XAS final states (quantified by the Slater integrals G_{pd}) is mainly responsible for differences in the $L_{3,2}$-edge branching ratios in PFY-XAS as compared to XAS and also for the suppression of the L_3 pre-edge[75] (herein called pre-edge peak). They argue that the exchange interaction orders the energy of XAS final states within the L-edge spectrum in accordance with their total angular momenta J, resulting in high-J states at the “low-energy side” (the pre-edge peak) of the L_3-edge and low-J states at the high energy side. The high-J states “tend to have lower fluorescence strengths, while there is no influence on the major (Auger) decay channel from these XAS final states”.[75] With this, the suppression of the pre-edge peak and the enhancement of the L_2-edge features in PFY-XAS as compared to XAS can be explained. As high-J states tend to have high total spin S, these findings are consistent with XAS spectrum analyses of $Mn^{II}(acac)_2$ and $Mn^{III}(acac)_3$ using RAS, revealing the ordering of XAS final states by their spin multiplicity (2S+1).[13] Comparisons of the calculated PFY-XAS to the XAS spectra from RAS in Figures 7C and 7D reproduce all observations discussed above. This confirms that in our RAS approach the intra-atomic effects responsible for state-dependent fluorescence yield are taken into account albeit with

Author Manuscript Author Manuscript Author Manuscript Author Manuscript

deviations in the calculated relative XAS versus PFY-XAS intensities at the L_2-edge compared to experiment.

Potentials of the Method for Highly Dilute Samples and Table-Top X-ray Sources

Based on an extrapolation of our results we now discuss the application of L-edge XAS with a transmission flatjet to other experimental designs with, first, low sample concentrations on the order of 1 mM as achieved for many biologically relevant samples[1, 12] and, second, with lower photon fluxes, as available for example from table-top soft x-ray sources.[76–83]

An important factor delimiting the quality of a spectrum is the signal-to-noise ratio (S/N). From the absorption spectra shown in Figure 3A we estimate that the relevant multiplet structures of a Mn L-edge spectrum are minimally resolved, if features with absorption signals of 1 Mb have a S/N≥1. From our measurements we identify two terms contributing to the total noise N of a transmission spectrum, namely the experimental noise N_{exp} due to detection and x-ray source noise and the "jet-noise" N_{jet} in case of an unstable operation of the transmission flatjet. We illustrate the meaning of the experimental noise N_{exp} and jet noise N_{jet} upon comparison of two exemplary single-scan spectra, one with the best and one of with the worst S/N, namely that of 15 mM and that of 100 mM $Mn^{III}(acac)_3$ in Figure 2C, respectively. These spectra have noise levels (1σ) of around 0.1 % and 0.6 %, respectively. The 0.1 % noise is equal to the experimental noise $N_{exp}=10^{-3}$, measured without any sample in the beam. This comparison implies that for a stable transmission flatjet N_{exp} dominates the total noise N (in particular if the influence of thickness variations in the transmission flatjet is negligible). The higher noise level in the spectrum of the 100 mM sample is due to the notably less stable operation of the liquid flatjet (e.g. due to precipitation of the sample) where N_{jet} becomes the predominant term to the total noise. A third term, the statistical noise or shot noise N_{stat} is negligible under our experimental conditions, but can gain predominant character if lower photon fluxes or larger sample thicknesses are used. While N_{exp} and N_{jet} are extracted from our experimental observations and are herein assumed to be constant, the shot noise $N_{stat} = \sqrt{p_{out}}$ is determined by the number of photons $p_{out}=p_{in}\cdot\exp(-L/\Lambda_{solv})$ to be detected by the photodiode. It is parametrized via the number of photons incident on the sample p_{in}, the sample thickness L and the attenuation length of the solvent Λ_{solv} (here $\Lambda_{ethanol}$ at 640 eV equals 1.44 μm[46–47]). In Figure 8A, N_{stat} was calculated for 10^{12} photons per spectrum data point (corresponding to 1 s integration time with our experimental flux of 10^{12} photons/s) and a lower number of 10^4 photons per spectrum data point (which would correspond, e.g., to 1 s integration time with a flux of 10^4 photons/s). For our experimental conditions (with sample thicknesses around 3 μm and 10^{12} photons per data point) Figure 8A illustrates that $N_{stat} \ll (N_{exp}, N_{jet})$, i.e. that our measured S/N is not limited by statistical noise but rather by the experimental or jet noise contributions, respectively.

In Figure 8A we compare the expected amplitudes of the L-edge XAS signal dip S (green solid lines) of a 1 Mb feature for variable sample concentrations and sample thickness to the magnitudes of the noise terms N_{exp}, N_{jet} and N_{stat} (dashed, dotted and dash-dotted). The expected signal amplitudes $S=T_{dip}(L, c)=[1-\exp(-L\cdot c\cdot\sigma\cdot N_A)]$ are derived from Beer-Lambert's law. Our experimental 1 Mb signals (circle marks) measured with 10^{12} photons/s

Author Manuscript Author Manuscript Author Manuscript Author Manuscript

and at thicknesses around 3 μm agree well with the calculated amplitudes. This is also consistent with previous work measured with the transmission flatjet.[36]

Along the vertical axis of Figure 8A we observe that signal amplitudes decrease with decreasing concentrations and assuming a constant noise level this also implies that the S/N decreases. We can use this plot to estimate, for a given sample thickness, the feasibility of measuring meaningful Mn L-edge spectra (here in ethanol solution) of samples with different concentrations in the transmission flatjet, using the simple criterion $S \geq N$ where N is the dominant noise term. With this we expect that, assuming a stable flatjet (correspondingly with a dominant noise term N_{exp}) with a typical thickness of 3 μm, measurements for sample concentrations ranging from several 100 mM down to the order of 10 mM are feasible within a single scan.

For highly dilute biological samples with concentrations on the order of 1 mM with Figure 8A we expect that measuring a sufficiently resolved single-scan spectrum is unfeasible under our experimental conditions, since $S<N_{exp}$. At a sample thickness of around 3μm one would need to average around 25 single-scan spectra (each with $S/N_{exp}=0.2$) to increase the effective S/N to a minimum value of 1. In our experiment, this would correspond to around 4 h of data acquisition and a total sample consumption on the order of 1 liter, where we assume that no sample recycling unit is employed.[34] Sample consumption, however, is a limiting factor in spectroscopy of many precious samples such as biologically relevant complexes and metalloenzymes. Solutions of metalloproteins, in particular, are often available in volumes on the order of 1 ml only. Such measurements therefore rather require slowly flowing liquid jets with flow rates on the order of 1 μl/min[12] or sophisticated sample recovery systems for the transmission flatjet.[34] The latter would need to be optimized for recycling and rehydrating sensitive solution samples after exposure to vacuum and the probing x-rays to constantly guarantee unspoiled sample conditions.

Along the horizontal axis of Figure 8A the signal amplitudes increase with increasing sample thickness. If the dominant noise stays largely constant, a different way to increase S/N of low concentrated samples would therefore lie in increasing the sample thickness and therefore also S/N. However, this concept is limited by the increased absorption by the solvent, which leads to an increased shot noise N_{stat} and to a decreased detector signal, saturating close to the zero-level of the detector. The former effect is estimated in Figure 8A, where at large sample thicknesses we expect $N_{stat}>S$. The latter effect is illustrated in Figure 8B for some typical solvents, assuming our experimental conditions at 10^{12} photons/s, where at thicknesses between 10 and 30 μm the transmitted signal (colored lines) dips below the detection limit of our detector (gray dotted line).

We now turn our discussion to applications of L-edge XAS on the transmission flatjet using table-top soft x-ray sources[77, 79–83] which have mostly lower average flux than used in our study. For example, earlier implementations of soft x-ray sources based on high harmonic generation provide on the order of 10^4 photons/s in the spectrum range and spectral bandwidth used in our study.[76, 78] With Figure 8A we expect that reducing the photon flux delimits the parameter space where our method provides single-scan spectra with $S/N>1$, as the statistical noise N_{stat} is increased. For sample thicknesses around 3μm we expect this

Author Manuscript Author Manuscript Author Manuscript Author Manuscript

experimental feasibility for sample concentrations on the order of several 100 mM and larger.

The statistical noise N_{stat} defines the theoretical limits of experimental feasibility where all other noise sources are eliminated. We use it to calculate the minimum number of photons that is required per spectrum data point for recording L-edge XAS of Mn solution samples in a transmission flatjet under ideal conditions (stable flatjet in particular). In Figure 8C we plot this minimum number of incident photons $p_{min}(L, c, \Lambda_{solv}) = [(1 - \exp(-L \cdot c \cdot \sigma \cdot N_A))^2 \cdot \exp(-L/\Lambda_{solv})]^{-1}$ for variable sample concentration and thickness. For these estimates we used $\Lambda_{ethanol}(640\ eV)=1.44\ \mu m$ and used the above criterion that a 1 Mb feature is resolved with $S/N_{stat}=1$.

Three major observations can be made in Figure 8C. First, in an ideal experiment acquisition of Mn L-edge XAS in a transmission flatjet is most efficient at a sample thickness at $L_{min}=2.9\ \mu m$ (for ethanol) independent of the sample concentration. This coincides with the flatjet thicknesses used in our experiments. Our above discussion, however, shows that with our non-ideal experimental noise it is favorable to increase the sample thickness beyond L_{min}. Second, for a given photon number per spectrum data point one can read off the theoretical minimum in sample concentration which in an ideal experiment could be measured with S/N>1 in a single-scan. For example, for soft x-ray sources with a flux on the order of 10^4 photons/s, this would be expected for sample concentrations on the order of a few 100 mM. Third, the figure shows that in an ideal experiment where only statistical noise contributes, measuring absorption spectra of samples with concentrations as low as 1 mM may be detectable already with 10^9 photons per spectrum data point. Reaching such ideal experimental conditions will require further reduction of the experimental (detection and x-ray source) and jet-induced noise sources.

IV. Conclusions

In this paper we present results from L-edge x-ray absorption spectroscopy of dilute transition metal complexes in solution using a transmission flatjet. We show that this approach is ideally suited for probing dilute radiation sensitive transition metal complexes in solution, here for $Mn^{II}(acac)_2$ and $Mn^{III}(acac)_3$, as we strictly avoid x-ray induced sample damage with fast sample replenishment. We show that the method allows extracting important information on the absolute absorption cross sections. We use this to demonstrate that within the experimental uncertainty the integrated absorption cross sections of Mn^{III} with respect to Mn^{II} are consistent with the ratio expected from the number of holes in the 3d shells of the two systems. In future studies with better S/N this could be extended to assess the ionic or covalent character of the metal-ligand bonds. Our measured Mn L-edge peak cross-sections of 12 and 9 Mb for $Mn^{II}(acac)_2$ and $Mn^{III}(acac)_3$, respectively, can be used to plan future Mn L-edge experiments. Comparison of our experimental spectra to crystal field and charge transfer multiplet calculations shows that the occurrence of a weak/strong pre-edge peak at around 1 to 2 eV below the L_3 absorption maximum is characteristic for tetrahedral/(nearly) octahedral ligand environments in Mn^{II} and Mn^{III}. For the Mn^{II} complex and to a weaker extent for the Mn^{III} complex, we find evidence for charge transfer states on the high-energy side of the L_3-edge. We show that L-edge absorption spectra from

Author Manuscript Author Manuscript Author Manuscript Author Manuscript

ab-initio restricted active space calculations reproduce the experimental spectra with very good agreement with respect to shapes, relative absorption strengths, peak positions as well as the oxidation-state dependent Mn^{II}-Mn^{III} shift. The experimentally observed enhancement and suppression of features in fluorescence-detected x-ray absorption spectra (partial fluorescence yield) as compared to absorption cross section spectra due to state-dependent fluorescence yield is correctly reproduced by the RAS calculations. We discuss the potential of further L-edge XAS experiments of dilute 3d metal complexes in solution with a transmission flatjet. Under the present experimental conditions with a relative noise level of 10^{-3} in flux transmitted by the sample and at a high-brilliance undulator beamline at a synchrotron radiation source the approach is shown to be suited for studies of 3d transition metal complexes in solution with concentrations from several 100 mM to several 10 mM. We estimate the feasibility of transferring our approach to table-top soft x-ray sources with sample concentrations on the order of several 100 mM. We further expect that under the present conditions studies of biological samples with metal concentrations around 1 mM impose severe experimental challenges.

Supplementary Material

Refer to Web version on PubMed Central for supplementary material.

Acknowledgments

We gratefully acknowledge the continuous support by the BESSY II staff and we thank HZB for the allocation of synchrotron radiation beamtime. We thank W. Quevedo (HZB) and C. Weniger (HZB) for support during set up and K. Holldack (HZB) for helpful discussions on the noise sources. We acknowledge financial support from Human Frontiers Science Program (RGP0063/2013), the Swedish Research Council, and the Knut and Alice Wallenberg Foundation (Grant No. KAW-2013.0020), and the German Science Foundation (Project No. DFG-NI 492/11-1). The computations were performed on resources provided by SNIC through Uppsala Multidisciplinary Center for Advanced Computational Science (UPPMAX) under project snic2016-1-464 and National Supercomputer Centre at Linköping University (Triolith) under project snic2016-1-508. The SSRL Structural Molecular Biology Program (T.K.) is supported by the DOE Office of Biological and Environmental Research, and by the National Institutes of Health, National Institute of General Medical Sciences (including P41GM103393). Parts of this research is supported by the Director, Office of Science, Office of Basic Energy Sciences, Division of Chemical Sciences, Geosciences, and Biosciences of the Department of Energy under contract DE-AC02-05CH11231 (J.Y., V.K.Y.), and by the NIH Grants GM110501 (J.Y.), GM126289 (J.K.) and GM55302 (V.K.Y).

References

1. Yano J, Yachandra V. Mn4Ca Cluster in Photosynthesis: Where and How Water is Oxidized to Dioxygen. Chemical Reviews. 2014; 114(8):4175–4205. [PubMed: 24684576]
2. Fritsch J, Scheerer P, Frielingsdorf S, Kroschinsky S, Friedrich B, Lenz O, Spahn CM. The crystal structure of an oxygen-tolerant hydrogenase uncovers a novel iron-sulphur centre. Nature. 2011; 479(7372):249–52. [PubMed: 22002606]
3. Seefeldt LC, Hoffman BM, Dean DR. Electron transfer in nitrogenase catalysis. Curr Opin Chem Biol. 2012; 16(1–2):19–25. [PubMed: 22397885]
4. Cramer SP, DeGroot FMF, Ma Y, Chen CT, Sette F, Kipke CA, Eichhorn DM, Chan MK, Armstrong WH. Ligand field strengths and oxidation states from manganese L-edge spectroscopy. Journal of the American Chemical Society. 1991; 113(21):7937–7940.
5. De Groot FMF. X-ray absorption and dichroism of transition metals and their compounds. Journal of Electron Spectroscopy and Related Phenomena. 1994; 67(4):529–622.
6. Grush MM, Chen J, Stemmler TL, George SJ, Ralston CY, Stibrany RT, Gelasco A, Christou G, Gorun SM, Penner-Hahn JE, Cramer SP. Manganese L-Edge X-ray Absorption Spectroscopy of

Author Manuscript Author Manuscript Author Manuscript Author Manuscript

Manganese Catalase from Lactobacillus plantarum and Mixed Valence Manganese Complexes. Journal of the American Chemical Society. 1996; 118(1):65–69.

7. Wasinger EC, de Groot FMF, Hedman B, Hodgson KO, Solomon EI. L-edge X-ray Absorption Spectroscopy of Non-Heme Iron Sites: Experimental Determination of Differential Orbital Covalency. Journal of the American Chemical Society. 2003; 125(42):12894–12906. [PubMed: 14558838]
8. Hocking RK, Wasinger EC, De Groot FMF, Hodgson KO, Hedman B, Solomon EI. Fe L-edge XAS studies of K4[Fe(CN)6] and K 3[Fe(CN)6]: A direct probe of back-bonding. Journal of the American Chemical Society. 2006; 128(32):10442–10451. [PubMed: 16895409]
9. Hocking RK, Wasinger EC, Yan Y-L, de Groot FMF, Walker FA, Hodgson KO, Hedman B, Solomon EI. Fe L-Edge X-ray Absorption Spectroscopy of Low-Spin Heme Relative to Non-heme Fe Complexes: Delocalization of Fe d-Electrons into the Porphyrin Ligand. Journal of the American Chemical Society. 2007; 129(1):113–125. [PubMed: 17199290]
10. Wilson SA, Kroll T, Decreau RA, Hocking RK, Lundberg M, Hedman B, Hodgson KO, Solomon EI. Iron L-edge X-ray absorption spectroscopy of oxy-picket fence porphyrin: experimental insight into Fe-O2 bonding. J Am Chem Soc. 2013; 135(3):1124–36. [PubMed: 23259487]
11. Kunnus K, Zhang W, Delcey MG, Pinjari RV, Miedema PS, Schreck S, Quevedo W, Schroder H, Fohlisch A, Gaffney KJ, Lundberg M, Odelius M, Wernet P. Viewing the Valence Electronic Structure of Ferric and Ferrous Hexacyanide in Solution from the Fe and Cyanide Perspectives. J Phys Chem B. 2016; 120(29):7182–94. [PubMed: 27380541]
12. Kubin M, Kern J, Gul S, Kroll T, Chatterjee R, Löchel H, Fuller FD, Sierra RG, Quevedo W, Weniger C, Rehanek J, Firsov A, Laksmono H, Weninger C, Alonso-Mori R, Nordlund DL, Lassalle-Kaiser B, Glownia JM, Krzywinski J, Moeller S, Turner JJ, Minitti MP, Dakovski GL, Koroidov S, Kawde A, Kanady JS, Tsui EY, Suseno S, Han Z, Hill E, Taguchi T, Borovik AS, Agapie T, Messinger J, Erko A, Föhlisch A, Bergmann U, Mitzner R, Yachandra VK, Yano J, Wernet P. Soft x-ray absorption spectroscopy of metalloproteins and high-valent metal-complexes at room temperature using free-electron lasers. Structural Dynamics. 2017; 4(5):054307. [PubMed: 28944255]
13. Kubin, M., Guo, M., Kroll, T., Löchel, H., Källman, E., Baker, ML., Mitzner, R., Gul, S., Kern, J., Föhlisch, A., Erko, A., Bergmann, U., Yachandra, V., Yano, J., Lundberg, M., Wernet, P. Probing the Oxidation State of Transition Metal Complexes: A Case Study on How Charge and Spin Densities Determine Mn L-Edge X-ray Absorption Energies. 2018. (submitted)
14. Yang BX, Kirz J. Extended x-ray-absorption fine structure of liquid water. Physical Review B. 1987; 36(2):1361–1364.
15. Näslund LÅ, Lüning J, Ufuktepe Y, Ogasawara H, Wernet P, Bergmann U, Pettersson LGM, Nilsson A. X-ray Absorption Spectroscopy Measurements of Liquid Water. The Journal of Physical Chemistry B. 2005; 109(28):13835–13839. [PubMed: 16852732]
16. Nagasaka M, Hatsui T, Horigome T, Hamamura Y, Kosugi N. Development of a liquid flow cell to measure soft X-ray absorption in transmission mode: A test for liquid water. Journal of Electron Spectroscopy and Related Phenomena. 2010; 177(2–3):130–134.
17. Huse N, Kim TK, Jamula L, McCusker JK, de Groot FMF, Schoenlein RW. Photo-Induced Spin-State Conversion in Solvated Transition Metal Complexes Probed via Time-Resolved Soft X-ray Spectroscopy. Journal of the American Chemical Society. 2010; 132(19):6809–6816. [PubMed: 20426414]
18. Schreck S, Gavrila G, Weniger C, Wernet P. A sample holder for soft x-ray absorption spectroscopy of liquids in transmission mode. Rev Sci Instrum. 2011; 82(10):103101. [PubMed: 22047274]
19. Aziz EF, Freiwald M, Eisebitt S, Eberhardt W. Steric hindrance of ion-ion interaction in electrolytes. Physical Review B. 2006; 73(7):075120.
20. Schön D, Golnak R, Tesch MF, Winter B, Velasco-Velez J-J, Aziz EF, Xiao J. Bulk-Sensitive Detection of the Total Ion Yield for X-ray Absorption Spectroscopy in Liquid Cells. The Journal of Physical Chemistry Letters. 2017:5136–5140. [PubMed: 28980813]
21. Yano J, Kern J, Irrgang KD, Latimer MJ, Bergmann U, Glatzel P, Pushkar Y, Biesiadka J, Loll B, Sauer K, Messinger J, Zouni A, Yachandra VK. X-ray damage to the Mn4Ca complex in single

Author Manuscript Author Manuscript Author Manuscript Author Manuscript

crystals of photosystem II: a case study for metalloprotein crystallography. Proc Natl Acad Sci U S A. 2005; 102(34):12047–52. [PubMed: 16103362]

22. van Schooneveld MM, DeBeer S. A close look at dose: Toward L-edge XAS spectral uniformity, dose quantification and prediction of metal ion photoreduction. Journal of Electron Spectroscopy and Related Phenomena. 2015; 198:31–56.
23. Titus CJ, Baker ML, Lee SJ, Cho H-M, Doriese WB, Fowler JW, Gaffney K, Gard JD, Hilton GC, Kenney C, Knight J, Li D, Marks R, Minitti MP, Morgan KM, O'Neil GC, Reintsema CD, Schmidt DR, Sokaras D, Swetz DS, Ullom JN, Weng T-C, Williams C, Young BA, Irwin KD, Solomon EI, Nordlund D. L-edge spectroscopy of dilute, radiation-sensitive systems using a transition-edge-sensor array. The Journal of Chemical Physics. 2017; 147(21):214201. [PubMed: 29221417]
24. Faubel M, Schlemmer S, Toennies JP. A molecular beam study of the evaporation of water from a liquid jet. Zeitschrift für Physik D Atoms, Molecules and Clusters. 1988; 10(2):269–277.
25. Wilson KR, Rude BS, Catalano T, Schaller RD, Tobin JG, Co DT, Saykally RJ. X-ray Spectroscopy of Liquid Water Microjets. The Journal of Physical Chemistry B. 2001; 105(17): 3346–3349.
26. Kunnus K, Rajkovic I, Schreck S, Quevedo W, Eckert S, Beye M, Suljoti E, Weniger C, Kalus C, Grubel S, Scholz M, Nordlund D, Zhang W, Hartsock RW, Gaffney KJ, Schlotter WF, Turner JJ, Kennedy B, Hennies F, Techert S, Wernet P, Fohlisch A. A setup for resonant inelastic soft x-ray scattering on liquids at free electron laser light sources. Rev Sci Instrum. 2012; 83(12):123109. [PubMed: 23277974]
27. Wernet P, Kunnus K, Schreck S, Quevedo W, Kurian R, Techert S, de Groot FM, Odelius M, Fohlisch A. Dissecting Local Atomic and Intermolecular Interactions of Transition-Metal Ions in Solution with Selective X-ray Spectroscopy. J Phys Chem Lett. 2012; 3(23):3448–53. [PubMed: 26290971]
28. Winter B. Liquid microjet for photoelectron spectroscopy. Nuclear Instruments and Methods in Physics Research Section A: Accelerators, Spectrometers, Detectors and Associated Equipment. 2009; 601(1):139–150.
29. Hocking RK, DeBeer George S, Raymond KN, Hodgson KO, Hedman B, Solomon EI. Fe L-Edge X-ray Absorption Spectroscopy Determination of Differential Orbital Covalency of Siderophore Model Compounds: Electronic Structure Contributions to High Stability Constants. Journal of the American Chemical Society. 2010; 132(11):4006–4015. [PubMed: 20187651]
30. De Groot, F., Kotani, A. Core level spectroscopy of solids. CRC Press; Boka Raton, USA: 2008.
31. de Groot FMF, Arrio MA, Sainctavit P, Cartier C, Chen CT. Fluorescence yield detection: Why it does not measure the X-ray absorption cross section. Solid State Communications. 1994; 92(12): 991–995.
32. Kurian R, Kunnus K, Wernet P, Butorin SM, Glatzel P, de Groot FM. Intrinsic deviations in fluorescence yield detected x-ray absorption spectroscopy: the case of the transition metal L(2),(3) edges. J Phys Condens Matter. 2012; 24(45):452201. [PubMed: 23060535]
33. Achkar AJ, Regier TZ, Wadati H, Kim YJ, Zhang H, Hawthorn DG. Bulk sensitive x-ray absorption spectroscopy free of self-absorption effects. Physical Review B. 2011; 83(8)
34. Ekimova M, Quevedo W, Faubel M, Wernet P, Nibbering ET. A liquid flatjet system for solution phase soft-x-ray spectroscopy. Struct Dyn. 2015; 2(5):054301. [PubMed: 26798824]
35. Ekimova M, Quevedo W, Szyc Ł, Iannuzzi M, Wernet P, Odelius M, Nibbering ETJ. Aqueous Solvation of Ammonia and Ammonium: Probing Hydrogen Bond Motifs with FT-IR and Soft X-ray Spectroscopy. Journal of the American Chemical Society. 2017; 139(36):12773–12783. [PubMed: 28810120]
36. Fondell M, Eckert S, Jay RM, Weniger C, Quevedo W, Niskanen J, Kennedy B, Sorgenfrei F, Schick D, Giangrisostomi E, Ovsyannikov R, Adamczyk K, Huse N, Wernet P, Mitzner R, Föhlisch A. Time-resolved soft X-ray absorption spectroscopy in transmission mode on liquids at MHz repetition rates. Structural Dynamics. 2017; 4(5):054902. [PubMed: 28852689]
37. de Groot FMF, Fuggle JC, Thole BT, Sawatzky GA. 2px-ray absorption of 3dtransition-metal compounds: An atomic multiplet description including the crystal field. Physical Review B. 1990; 42(9):5459–5468.

Author Manuscript Author Manuscript Author Manuscript Author Manuscript

38. Groot, Fd. Multiplet effects in X-ray spectroscopy. Coordination Chemistry Reviews. 2005; 249(1–2):31–63.
39. Josefsson I, Kunnus K, Schreck S, Föhlisch A, de Groot F, Wernet P, Odelius M. Ab Initio Calculations of X-ray Spectra: Atomic Multiplet and Molecular Orbital Effects in a Multiconfigurational SCF Approach to the L-Edge Spectra of Transition Metal Complexes. The Journal of Physical Chemistry Letters. 2012; 3(23):3565–3570. [PubMed: 26290989]
40. Pinjari RV, Delcey MG, Guo M, Odelius M, Lundberg M. Restricted active space calculations of L-edge X-ray absorption spectra: from molecular orbitals to multiplet states. J Chem Phys. 2014; 141(12):124116. [PubMed: 25273421]
41. Malmqvist PÅ, Roos BO, Schimmelpfennig B. The restricted active space (RAS) state interaction approach with spin-orbit coupling. Chemical Physics Letters. 2002; 357(3–4):230–240.
42. Malmqvist PÅ, Pierloot K, Shahi ARM, Cramer CJ, Gagliardi L. The restricted active space followed by second-order perturbation theory method: Theory and application to the study of CuO2 and Cu 2O2 systems. Journal of Chemical Physics. 2008; 128(20)
43. Preuße M, Bokarev SI, Aziz SG, Kühn O. Towards an ab initio theory for metal L-edge soft X-ray spectroscopy of molecular aggregates. Structural Dynamics. 2016; 3(6):062601. [PubMed: 27679809]
44. Bokarev SI, Khan M, Abdel-Latif MK, Xiao J, Hilal R, Aziz SG, Aziz EF, Kühn O. Unraveling the Electronic Structure of Photocatalytic Manganese Complexes by L-Edge X-ray Spectroscopy. The Journal of Physical Chemistry C. 2015; 119(33):19192–19200.
45. Miedema PS, Quevedo W, Fondell M. The variable polarization undulator beamline UE52 SGM at BESSY II. Journal of large-scale research facilities JLSRF. 2016; 2:70.
46. Henke BL, Gullikson EM, Davis JC. X-Ray Interactions: Photoabsorption, Scattering, Transmission, and Reflection at E = 50-30,000 eV, Z = 1-92. Atomic Data and Nuclear Data Tables. 1993; 54(2):181–342.
47. CXRO Center for X-ray Optics, X-ray Database. [accessed 06/01/2017] (http://henke.lbl.gov/optical_constants/)
48. Mitzner R, Rehanek J, Kern J, Gul S, Hattne J, Taguchi T, Alonso-Mori R, Tran R, Weniger C, Schröder H, Quevedo W, Laksmono H, Sierra RG, Han G, Lassalle-Kaiser B, Koroidov S, Kubicek K, Schreck S, Kunnus K, Brzhezinskaya M, Firsov A, Minitti MP, Turner JJ, Moeller S, Sauter NK, Bogan MJ, Nordlund D, Schlotter WF, Messinger J, Borovik A, Techert S, de Groot FMF, Föhlisch A, Erko A, Bergmann U, Yachandra VK, Wernet P, Yano J. L-Edge X-ray Absorption Spectroscopy of Dilute Systems Relevant to Metalloproteins Using an X-ray Free-Electron Laser. The Journal of Physical Chemistry Letters. 2013; 4(21):3641–3647. [PubMed: 24466387]
49. Forman A, Orgel LE. The Jahn-Teller effect in manganic acetylacetonate. Molecular Physics. 1959; 2(4):362–366.
50. Diaz-Acosta I, Baker J, Hinton JF, Pulay P. Calculated and experimental geometries and infrared spectra of metal tris-acetylacetonates: vibrational spectroscopy as a probe of molecular structure for ionic complexes. Part II. Spectrochimica Acta Part A: Molecular and Biomolecular Spectroscopy. 2003; 59(2):363–377.
51. Stults BR, Day RO, Marianelli RS, Day VW. Distortions of the coordination polyhedron in high-spin manganese(III) complexes. 2. Crystal structure of thiocyanatobis(acetylacetonato)manganese(III). Inorganic Chemistry. 1979; 18(7):1847–1852.
52. Lundberg M, Siegbahn PEM. Theoretical investigations of structure and mechanism of the oxygen-evolving complex in PSII. Physical Chemistry Chemical Physics. 2004; 6(20):4772–4780.
53. Shibata S, Onuma S, Inoue H. CRYSTAL STRUCTURE OF TRIMERIC BIS(ACETYLACETONATO)MANGANESE(II). Chemistry Letters. 1984; 13(4):485–486.
54. Guo M, Sorensen LK, Delcey MG, Pinjari RV, Lundberg M. Simulations of iron K pre-edge X-ray absorption spectra using the restricted active space method. Phys Chem Chem Phys. 2016; 18(4): 3250–9. [PubMed: 26742851]
55. Guo M, Källman E, Sørensen LK, Delcey MG, Pinjari RV, Lundberg M. Molecular Orbital Simulations of Metal 1s2p Resonant Inelastic X-ray Scattering. The Journal of Physical Chemistry A. 2016; 120(29):5848–5855. [PubMed: 27398775]

Author Manuscript Author Manuscript Author Manuscript Author Manuscript

56. Wernet P, Kunnus K, Josefsson I, Rajkovic I, Quevedo W, Beye M, Schreck S, Grubel S, Scholz M, Nordlund D, Zhang W, Hartsock RW, Schlotter WF, Turner JJ, Kennedy B, Hennies F, de Groot FM, Gaffney KJ, Techert S, Odelius M, Fohlisch A. Orbital-specific mapping of the ligand exchange dynamics of Fe(CO)5 in solution. Nature. 2015; 520(7545):78–81. [PubMed: 25832405]
57. Aquilante F, De Vico L, Ferre N, Ghigo G, Malmqvist PA, Neogrady P, Pedersen TB, Pitonak M, Reiher M, Roos BO, Serrano-Andres L, Urban M, Veryazov V, Lindh R. MOLCAS 7: the next generation. J Comput Chem. 2010; 31(1):224–47. [PubMed: 19499541]
58. Pinjari RV, Delcey MG, Guo M, Odelius M, Lundberg M. Cost and sensitivity of restricted active-space calculations of metal L-edge X-ray absorption spectra. Journal of Computational Chemistry. 2016; 37(5):477–486. [PubMed: 26502979]
59. Ohno M, van Riessen GA. Hole-lifetime width: a comparison between theory and experiment. Journal of Electron Spectroscopy and Related Phenomena. 2003; 128(1):1–31.
60. Thole BT, Van Der Laan G, Fuggle JC, Sawatzky GA, Karnatak RC, Esteva JM. 3d x-ray-absorption lines and the 3d94fn+1 multiplets of the lanthanides. Physical Review B. 1985; 32(8): 5107–5118.
61. Stavitski E, de Groot FMF. The CTM4XAS program for EELS and XAS spectral shape analysis of transition metal L edges. Micron. 2010; 41(7):687–694. [PubMed: 20637641]
62. Van der Laan G, Kirkman I. The 2p absorption spectra of 3d transition metal compounds in tetrahedral and octahedral symmetry. Journal of Physics: Condensed Matter. 1992; 4(16):4189.
63. Thole BT, van der Laan G. Branching ratio in x-ray absorption spectroscopy. Physical Review B. 1988; 38(5):3158–3171.
64. Lee N, Petrenko T, Bergmann U, Neese F, Debeer S. Probing valence orbital composition with iron Kβ x-ray emission spectroscopy. Journal of the American Chemical Society. 2010; 132(28):9715–9727. [PubMed: 20578760]
65. Beckwith MA, Roemelt M, Collomb MN, DuBoc C, Weng TC, Bergmann U, Glatzel P, Neese F, DeBeer S. Manganese Kbeta X-ray emission spectroscopy as a probe of metal-ligand interactions. Inorg Chem. 2011; 50(17):8397–409. [PubMed: 21805960]
66. Grush MM, Muramatsu Y, Underwood JH, Gullikson EM, Ederer DL, Perera RCC, Callcott TA. Soft X-ray emission and absorption—a comparative study on the sensitivity to oxidation state and ligand environment of transition metal complexes1. Journal of Electron Spectroscopy and Related Phenomena. 1998; 92(1–3):225–229.
67. Glatzel P, Bergmann U, Yano J, Visser H, Robblee JH, Gu W, De Groot FMF, Christou G, Pecoraro VL, Cramer SP, Yachandra VK. The electronic structure of Mn in oxides, coordination complexes, and the oxygen-evolving complex of photosystem II studied by resonant inelastic X-ray scattering. Journal of the American Chemical Society. 2004; 126(32):9946–9959. [PubMed: 15303869]
68. Carlotto S, Sambi M, Vittadini A, Casarin M. Mn(acac)2 and Mn(acac)3 complexes, a theoretical modeling of their L2, 3-edges X-ray absorption spectra. Polyhedron. 2017; 135:216–223.
69. Carlotto S, Floreano L, Cossaro A, Dominguez M, Rancan M, Sambi M, Casarin M. The electronic properties of three popular high spin complexes [TM(acac)3, TM = Cr, Mn, and Fe] revisited: an experimental and theoretical study. Physical Chemistry Chemical Physics. 2017
70. Haverkort MW, Zwierzycki M, Andersen OK. Multiplet ligand-field theory using Wannier orbitals. Physical Review B. 2012; 85(16):165113.
71. de Groot FMF, Hu ZW, Lopez MF, Kaindl G, Guillot F, Tronc M. Differences between L3 and L2 x-ray absorption spectra of transition metal compounds. The Journal of Chemical Physics. 1994; 101(8):6570.
72. Figgis BN. Ligand field theory. Comprehensive Coordination Chemistry. 1987; 1:213–279.
73. Piper T, Carlin RL. Crystal Spectra of Some Trisacetylacetonates. Inorganic Chemistry. 1963; 2(2): 260–263.
74. Yamaguchi K, Sawyer DT. Redox chemistry for the mononuclear tris(picolinato)-tris(acetylacetonata)-, and tris(8-quinolinata)manganese(III) complexes: reaction mimics for the water-oxidation cofactor in photosystem II. Inorganic Chemistry. 1985; 24(6):971–976.
75. Miedema PS, Wernet P, Föhlisch A. State-dependent fluorescence yields through the core-valence Coulomb exchange parameter. Physical Review A. 2014; 89(5)

Author Manuscript Author Manuscript Author Manuscript Author Manuscript

76. Seres E, Seres J, Krausz F, Spielmann C. Generation of Coherent Soft-X-Ray Radiation Extending Far Beyond the Titanium L Edge. Physical Review Letters. 2004; 92(16):163002. [PubMed: 15169224]

77. Fuchs M, Weingartner R, Popp A, Major Z, Becker S, Osterhoff J, Cortrie I, Zeitler B, Hörlein R, Tsakiris GD, Schramm U, Rowlands-Rees TP, Hooker SM, Habs D, Krausz F, Karsch S, Grüner F. Laser-driven soft-X-ray undulator source. Nature Physics. 2009; 5:826.

78. Popmintchev T, Chen M-C, Popmintchev D, Arpin P, Brown S, Ališauskas S, Andriukaitis G, Balčiunas T, Mücke OD, Pugzlys A, Baltuška A, Shim B, Schrauth SE, Gaeta A, Hernández-García C, Plaja L, Becker A, Jaron-Becker A, Murnane MM, Kapteyn HC. Bright Coherent Ultrahigh Harmonics in the keV X-ray Regime from Mid-Infrared Femtosecond Lasers. Science. 2012; 336(6086):1287. [PubMed: 22679093]

79. Cousin SL, Silva F, Teichmann S, Hemmer M, Buades B, Biegert J. High-flux table-top soft x-ray source driven by sub-2-cycle, CEP stable, 1.85-μm 1-kHz pulses for carbon K-edge spectroscopy. Opt Lett. 2014; 39(18):5383–5386. [PubMed: 26466278]

80. Mantouvalou I, Witte K, Grotzsch D, Neitzel M, Gunther S, Baumann J, Jung R, Stiel H, Kanngiesser B, Sandner W. High average power, highly brilliant laser-produced plasma source for soft X-ray spectroscopy. Rev Sci Instrum. 2015; 86(3):035116. [PubMed: 25832284]

81. Zhang K, Lin M-F, Ryland ES, Verkamp MA, Benke K, de Groot FMF, Girolami GS, Vura-Weis J. Shrinking the Synchrotron: Tabletop Extreme Ultraviolet Absorption of Transition-Metal Complexes. The Journal of Physical Chemistry Letters. 2016; 7(17):3383–3387. [PubMed: 27513100]

82. Attar AR, Bhattacherjee A, Pemmaraju CD, Schnorr K, Closser KD, Prendergast D, Leone SR. Femtosecond x-ray spectroscopy of an electrocyclic ring-opening reaction. Science. 2017; 356(6333):54. [PubMed: 28386006]

83. Pertot Y, Schmidt C, Matthews M, Chauvet A, Huppert M, Svoboda V, von Conta A, Tehlar A, Baykusheva D, Wolf J-P, Wörner HJ. Time-resolved x-ray absorption spectroscopy with a water window high-harmonic source. Science. 2017; 355(6322):264. [PubMed: 28059713]

Author Manuscript Author Manuscript Author Manuscript Author Manuscript

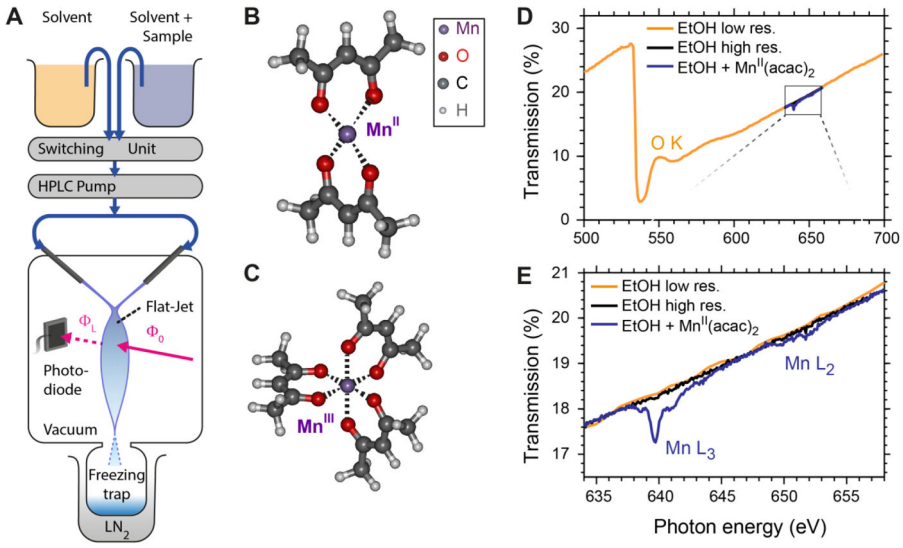

Figure 1.

(A) Schematic of the setup with the liquid flatjet system for L-edge x-ray absorption spectroscopy of transition metal complexes in solution. (B, C) Molecular structures of the studied complexes $Mn^{II}(acac)_2$ (B) and $Mn^{III}(acac)_3$ (C). (D) and (E) Transmission spectra of the pure solvent ethanol and 30 mM $Mn^{II}(acac)_2$ solution in ethanol, shown for the energy range of the oxygen K-edge (D) and the Mn L-edge (E), as acquired with 1 eV (“low res.”) and 0.1 eV step sizes (“high res.”), respectively. For comparison, the transmission curves in (D) and (E) were normalized with Beer-Lambert’s law to the thickness of the pure ethanol sample (2.44 μm).

Author Manuscript Author Manuscript Author Manuscript Author Manuscript

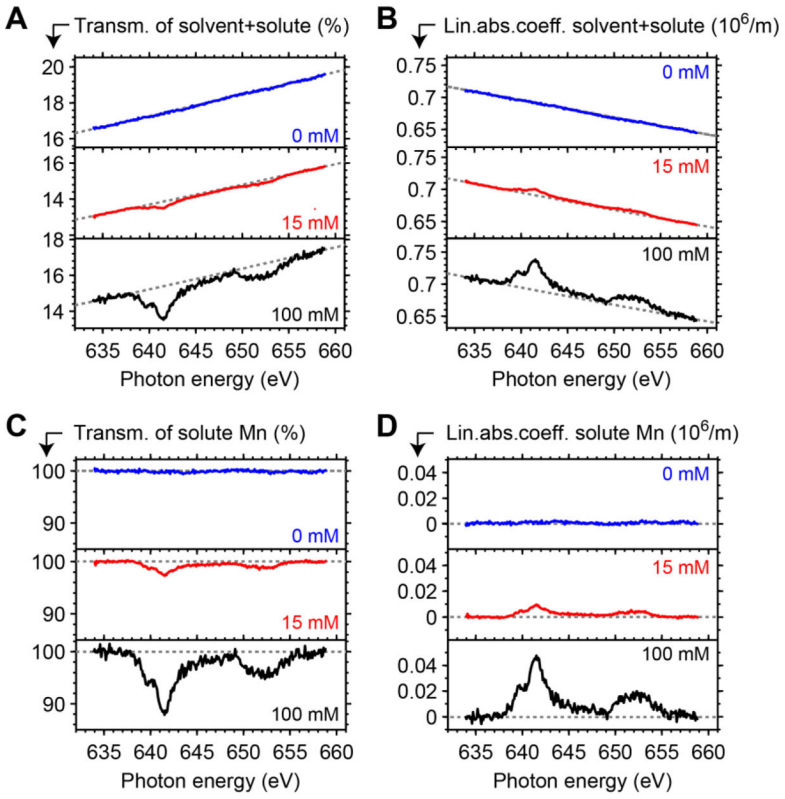

Figure 2.

Single scan spectra for Mn L-edge XAS of $Mn^{III}(acac)_3$ in ethanol solution as measured with the transmission flatjet. In all panels the Mn concentration increases from 0 mM (blue) to 15 mM (red) and 100 mM (black). (A) Experimental transmission spectra with sample thicknesses L of 2.5 μm (blue), 2.9 μm (red) and 2.7 μm (black). Gray dotted lines denote the fitted transmission of the solvent, as extracted from Henke's tables (see methods section). (B) Linear absorption coefficients α, as calculated from the data shown in (A). (C) Relative transmission dips associated with Mn L-edge absorption, obtained from division of the colored curves in (A) by the gray dotted solvent fits. (D) Linear absorption coefficients due to Mn L-edge absorption, obtained from subtraction of the gray dotted solvent fits from the colored curves in (B). The larger relative noise in the 100 mM data is due to a comparably unstable operation of the liquid flatjet during the scan.

Author Manuscript Author Manuscript Author Manuscript Author Manuscript

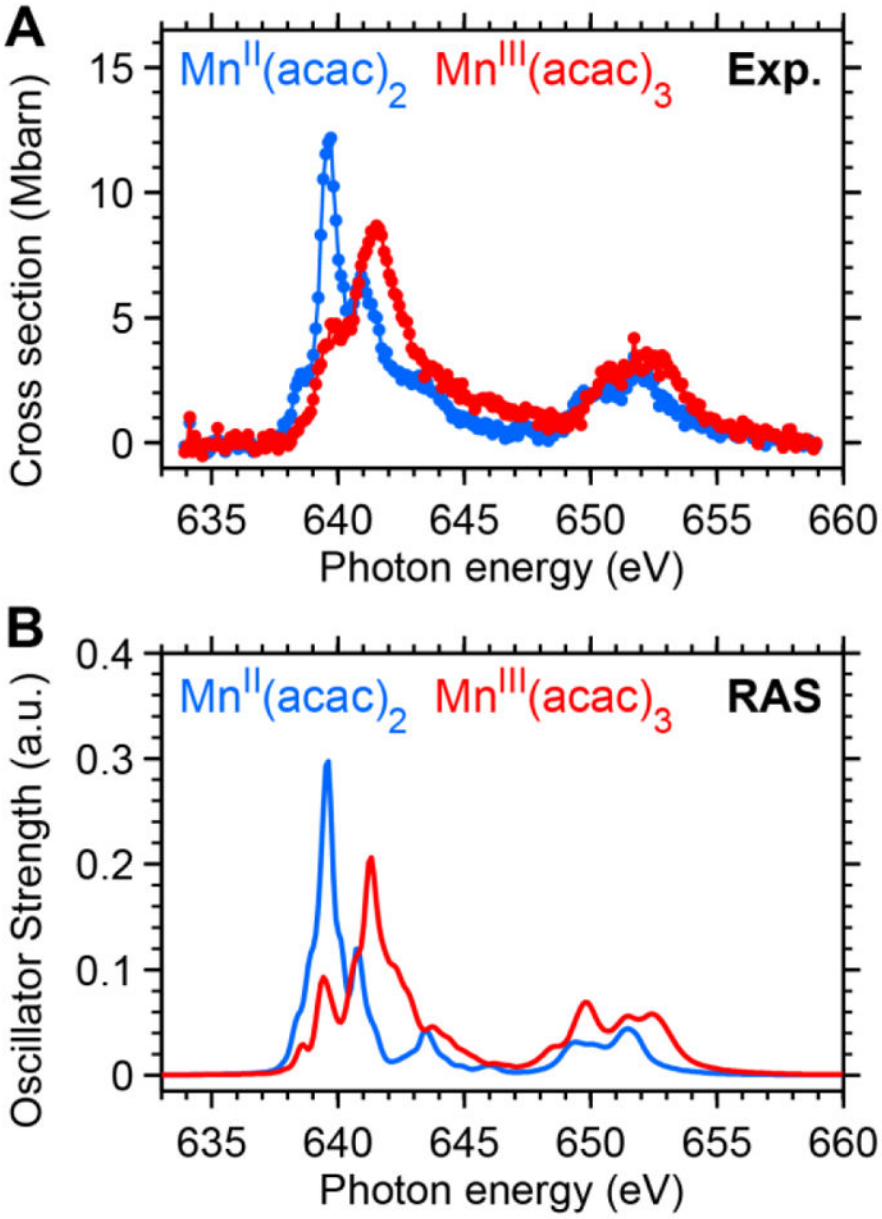

Figure 3.

Comparison of absolute L-edge XAS absorption cross sections of $Mn^{II}(acac)_2$ and $Mn^{III}(acac)_3$ in solution from (A) experiment and (B) ab-initio restricted active space (RAS) theory. The experimental spectra are averaged over several single-scan spectra and were calibrated in analogy to the PFY-XAS spectra in ref. 13. Both RAS spectra were calibrated using the same energy shift for coinciding L_3-edge peak positions in the RAS and the experimental spectra of $Mn^{II}(acac)_2$. The absorption amplitudes of experimental and RAS spectra are quantified in Table S2 in the Supporting Information.

Author Manuscript Author Manuscript Author Manuscript Author Manuscript

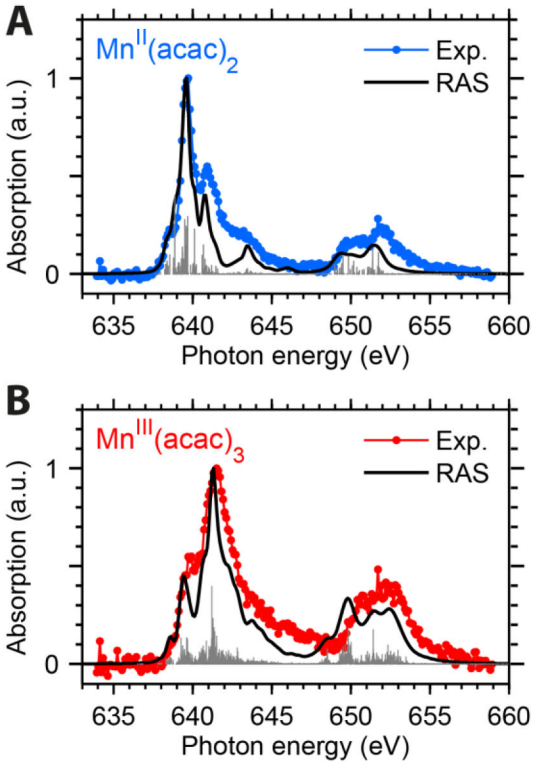

Figure 4.

Direct comparison of normalized spectra of (A) $Mn^{II}(acac)_2$ and (B) $Mn^{III}(acac)_3$ in solution from experiment (blue and red) and RAS theory (black lines) on a RASPT2 level. The sticks denote the transitions to individual XAS final states underlying to the RAS spectra. The energy axis of both RAS spectra was aligned with the same energy shift for coinciding L_3-edge peak positions in the experimental and the RAS spectra of $Mn^{II}(acac)_2$.

Author Manuscript Author Manuscript Author Manuscript Author Manuscript

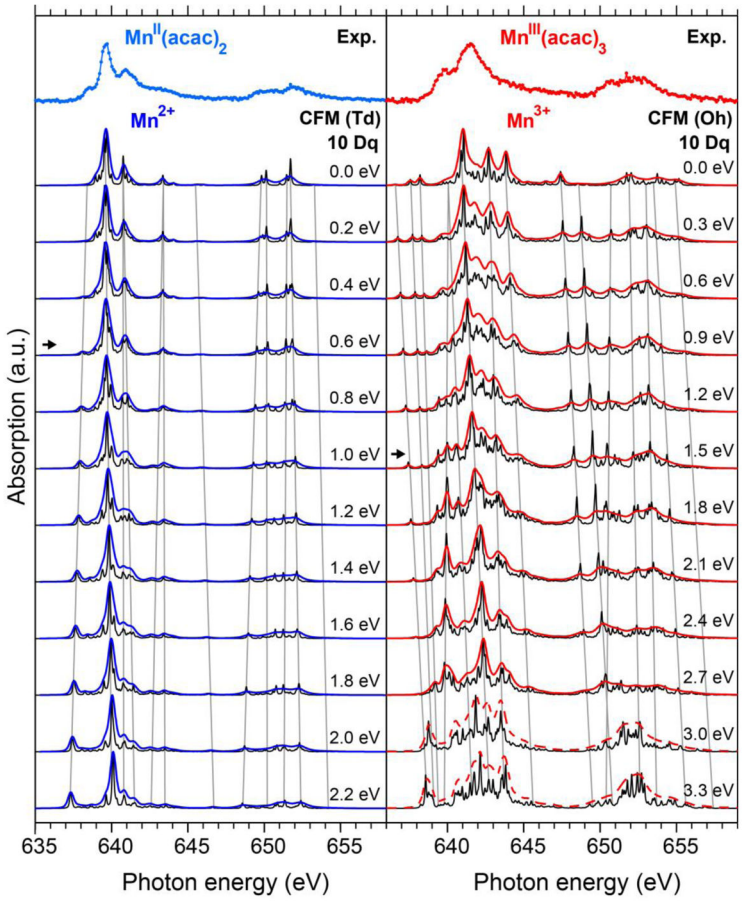

Figure 5.

Comparison of experimental L-edge XAS spectra of $Mn^{II}(acac)_2$ (top left) and $Mn^{III}(acac)_3$ (top right) to crystal field multiplet (CFM) calculations (rows 2 to 13) with a variable ligand field splitting (LFS) for Mn^{2+} (left) in T_d symmetry and Mn^{3+} (right) in O_h symmetry. The red and blue spectrum curves in rows 2–13 were calculated with the broadenings similar to the experimental values (see methods section). The black curves are broadened with a Lorentzian width 0.1 eV (FWHM) and a Gaussian width σ=0.01 eV for better discrimination of the underlying multiplet features. The experimental spectra are best reproduced by the CFM spectra marked with arrows. All CFM spectra of Mn^{2+} and Mn^{3+} have been shifted by the same constant offsets of −0.7 eV and −0.5 eV, respectively.

Author Manuscript Author Manuscript Author Manuscript Author Manuscript

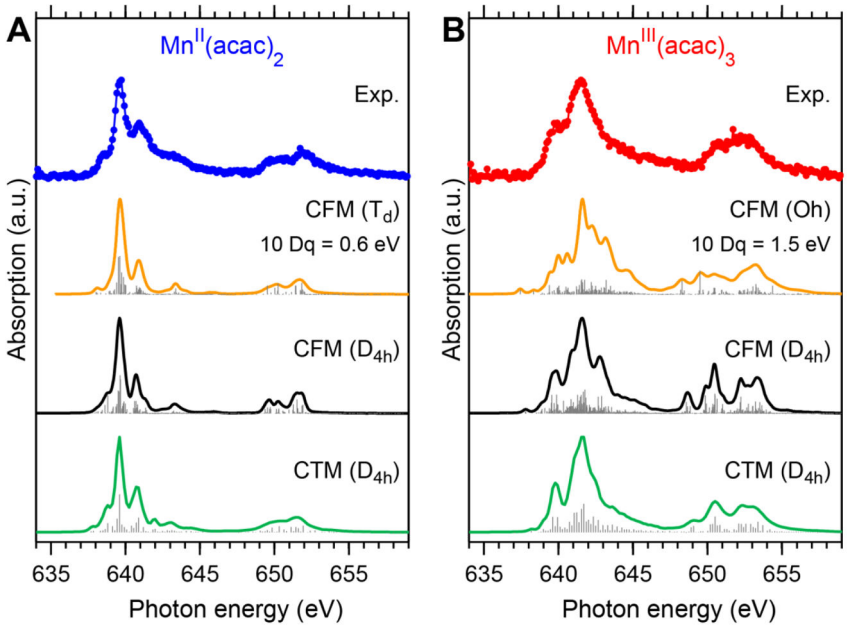

Figure 6.

Comparison of experimental spectra of $Mn^{II}(acac)_2$ (A) and $Mn^{III}(acac)_3$ (B) in solution to the best fitting CFM(T_d/O_h) spectra (orange) (arrows in Fig. 5) and those fitted with CFM(D_{4h}) (black) and CTM(D_{4h}) (green). The sticks denote the transitions to individual XAS final states underlying to the calculated spectra. The energy axis of all CFM and CTM spectra was aligned to that of the experimental spectra for coinciding L_3-edge peak-maximum positions. All fit parameters are given in Table S1 in the Supporting Information.

Author Manuscript Author Manuscript Author Manuscript Author Manuscript

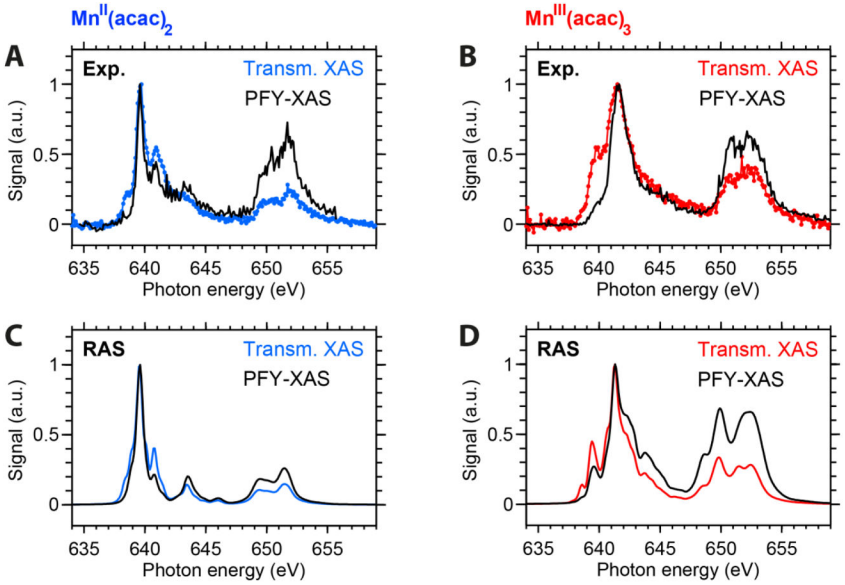

Figure 7.

Comparison of experimental and RAS-theoretical x-ray absorption spectra in transmission mode (XAS) and in partial fluorescence yield mode (PFY-XAS) for $Mn^{II}(acac)_2$ and $Mn^{III}(acac)_3$ in solution samples. Experimental and RAS calculated PFY-XAS spectra (black) are copied from ref. 13. All spectra are normalized to their peak intensity. The transmission XAS spectra in (A) and (B) were taken from Fig. 3A, those in (C) and (D) from Fig. 3B. Notably, the energy position of the features is conserved for both detection modes.

Author Manuscript Author Manuscript Author Manuscript Author Manuscript

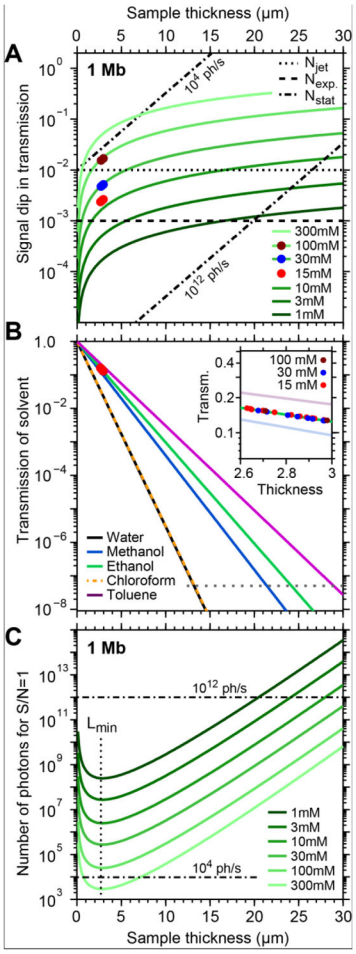

Figure 8.

Comparison of signal and noise amplitudes for L-edge XAS of dilute Mn complexes under our experimental conditions and in the theoretical limit. (A) Expected vs. experimental signal dips in transmission for a 1 Mb absorption feature at the Mn L-edge. The expected curves were derived for 640 eV photon energy and the solvent ethanol, using Henke's tables. The dashed/dotted lines assign the experimental and theoretical detection limits (see main text) for an acquisition time of 1 s per spectrum data point. (B) Transmission of typical solvents at the Mn L-edge (640 eV) with a magnification of the experimental range (inset). (C) Theoretical minimum number of incoming photons for detecting a 1 Mb absorption feature with S/N=1, here for statistical shot noise, using the solvent ethanol.